TOPIC REVIEW — Magnetism, magnetic materials, and interdisciplinary research

Spin plasmonics in magnetism*

Chui S T(徐少达)[a)†] and Lin Zhi-Fang(林志方)[a)b)]

[a)] *Bartol Research Institute, University of Delaware, Newark, DE* 19716, *USA*

[b)] *State Key Laboratory of Surface Physics and Department of Physics, Fudan University, Shanghai 200433, China*

(Received 26 July 2014; published online 20 October 2014)

We discuss a new class of phenomena that we call "spin plasmonics". It is motivated by three different recent trends of physics research: (i) spintronics, (ii) plasmonics, and (iii) topological properties as is exemplified by the quantized Hall effect. This involves the physics of the "magnetic surface plasmon" (MSP) which provides for an analog of the edge states discussed in the quantized Hall effect. Their properties can be easily tuned by an external magnetic field. They are coupled to the electromagnetic field and can be injected into metallic structures and induce spin and charge currents and hold the promise of miniturization of nonreciprocal devices.

Keywords: spin, plasmonics, magnetism, one way

PACS: 78.20.Ls, 42.70.Qs, 72.15.Gd, 73.43.–f **DOI:** 10.1088/1674-1056/23/11/117802

1. Introduction

One of the distinct properties of magnetic materials is their nonreciprocal behavior, which is due to the broken time reversal symmetry intrinsic in them. This unique characteristic has been exploited in many devices, such as circulators and isolators. In current designs, the sizes of these devices are of the order of the wavelengths of interest. A current theme of research is subwavelength structures. Surface plasmons (SP) are modes of electromagnetic (EM) radiations that are strongly coupled to collective oscillations of free-electrons at the interface of conductive materials. Resonances, such as the surface plasmon (SP), are found to enhance the transmission of electromagnetic waves through subwavelength holes in a metallic film.[1] The possibility that SP can provide a subwavelength transport of an electromagnetic (EM) wave has also been studied.[2–6] They enable the confinement of EM fields into subwavelength volumes with strong local field enhancement, which can be exploited to enhance light-matter interactions at the subwavelength scale, leading to a wide range of intriguing applications, such as active plasmonic devices,[7,8] biosensing,[9,10] and surface-enhanced spectroscopy.[11,12]

Because of the symmetry of Maxwell's equations with respect to its magnetic and electric degrees of freedom, there is a magnetic analog to the (electric) surface plasmon (SP), which on bulk surfaces is known as the Damon–Esbach mode.[13] We have found that the term magnetic surface plasmon (MSP) is more expressive and more general. Thus, we shall use it in this paper. MSPs hold the promise for subwavelength nonreciprocal devices.

The nonreciprocal nature of the MSP states are similar to that of electrons in the quantized Hall effect. Over the last ten years, there have been many studies on the effect of magnetic fields on the transport of electrons. An example is the quantized Hall effect, in which "edge states"[14] that behave like giant eddies which circulate around the edges of a sample, is believed to carry the current. These edge states are topological. They go only in one direction and have a finite Chern number.[15–17] The MSPs in a magnetic photonic crystal form a dense set of bands and exhibit increasing Chern numbers modulo the degree of rotation symmetry of the crystal.[18] The properties of the MSPs have an additional feature in that they can be easily tuned by an external magnetic field. They are coupled to the electromagnetic field and can be injected into metallic structures, and induce spin and charge currents. States such as the MSPs are the focus of the present paper. These states can potentially be exploited in spintronics devices with lower energy consumption than current ones.

In this paper, we describe some examples of the MSP excitations in different structures. Then, different physical phenomena related to the MSP will be described.

2. Excitation

2.1. "Bulk" MSP

To remind the readers why we call the Damon–Esbach mode the MSP, we recapitulate in Appendix A the derivations of the dispersions of the Damon–Esbach mode and the surface plasmons, so that the similarity of their derivation will be clear to the readers. Interests in this have been revived by recent spin polarized transport experiments[19–23] focusing on

*Project supported by the National Basic Research Program of China (Grant No. 2011CB922004) and the National Natural Science Foundation of China (Grant No. 11174059).

†Corresponding author. E-mail: chui@bartol.udel.edn

© 2014 Chinese Physical Society and IOP Publishing Ltd

the vertical structure with a layer of metal completely on top of YIG. We first recapitulate the bulk dispersion of the MSP, the Damon–Esbach mode.

The magnetic permeability tensor and its inverse are given by[24–26]

$$\hat{\mu} = \mu_0 \begin{bmatrix} \mu & -\mathrm{i}\mu' & 0 \\ \mathrm{i}\mu' & \mu & 0 \\ 0 & 0 & 1 \end{bmatrix}, \quad \hat{\mu}^{-1} = \begin{bmatrix} d & -\mathrm{i}b & 0 \\ \mathrm{i}b & d & 0 \\ 0 & 0 & 1 \end{bmatrix}, \qquad (1)$$

where μ and μ' are of the resonance form: $\mu = 1 + f_\mathrm{m}(f_0 + \mathrm{i}\alpha f)/[(f_0 + \mathrm{i}\alpha f)^2 - f^2]$, $\mu' = -f_\mathrm{m} f/[(f_0 + \mathrm{i}\alpha f)^2 - f^2]$ with a characteristic bare spin wave frequency $f_0 = \gamma H_0$. Here H_0 is a sum of the external field H_ext and the anisotropy field H_a, γ is the gyromagnetic ratio, $f_\mathrm{m} = \gamma 4\pi M_\mathrm{s}$ measures the coupling strength of the magnetic material with the EM waves, M_s is the saturation magnetization and α denotes the magnetic damping. $d = \mu/(\mu^2 - \mu'^2)$, $b = -\mu'/(\mu^2 - \mu'^2)$. For a magnetic insulator, such as YIG, $H_0 = 900$ Oe, $4\pi M_\mathrm{s} = 1750$ Oe, $\alpha = 7 \times 10^{-3}$, and the permittivity $\varepsilon_\mathrm{s} = 15 + \mathrm{i}7 \times 10^{-3}$.[25,26]

The frequency of the MSP at the air-YIG interface as a function of the wave vector k_x for the above parameters is illustrated in Fig. 1. This band lies in the bulk spin wave gap at long wavelengths above the spin wave frequency $f_\mathrm{sw} = 2\pi\omega_\mathrm{sw}$ observed in typical ferromagnetic (fmr) experiments

$$f_\mathrm{sw} = \sqrt{f_0(f_0 + f_\mathrm{m})}. \qquad (2)$$

The (electric) surface plasmon of infinite wave vector occurs at a frequency f_sp such that $\varepsilon = -1$. Similarly, at the MSP frequency,

$$f_\mathrm{s} = f_0 + f_\mathrm{m}/2, \qquad (3)$$

the effective magnetic permeability for one of the circular polarizations, $\mu_\mathrm{eff} = \mu - \mu'$ is equal to -1. This corresponds to a mode of infinite wave vector and forms the upper limit of the MSP band. Physically, $\mu_\mathrm{eff} = -1$ ($\varepsilon = -1$) corresponds to the Mie scattering resonance of all angular momenta $n > 0$ (n) of a 2D circular cylinder for TM (TE) modes in the long wavelength limit. The group velocities v_MSP of the MSP are of the order of 10^8 cm/s. The distance traveled is controlled by the damping coefficient α and is of the order $v_\mathrm{MSP}/(\alpha\omega)$.

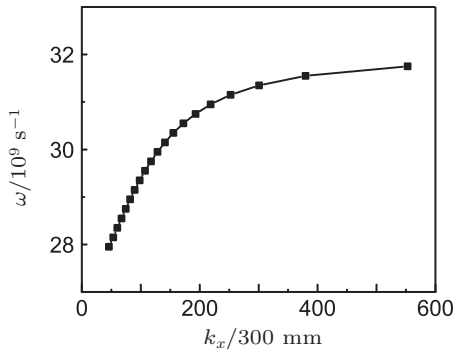


Fig. 1. The dispersion of the MSP at the surface of YIG.

When the dielectric constant ε_s is larger than one, there is another branch with $k_x < 0$. This is the case for the ferrite. This mode has not been taken into account in most recent works.

A MSP is a mixture of a spin wave and an EM wave localized near the interface. The spin wave amplitude decays exponentially as a function of $|y|$. The spins rotate longitudinally with components perpendicular to the YIG surface and along the direction of propagation. These two components are ninety degrees out of phase. A spin wave state localized near the surface with a width of the order of an exchanged length has been discussed theoretically recently by Xiao and Bauer.[27] The effect of the dipolar interaction is included with the constraint that the curl of H and the divergence of B inside the ferromagnet is equal to zero.[28] As is explained in Appendix A, the MSP is obtained from the constraint of the continuity of $B_\perp$ and $H_\parallel$ across the interface with the full electromagnetic wave dispersion taken into account. (Beyond the quasi-static limit.) This was not included in this theoretical calculation. As a result, the electric field is not coupled to the surface spin wave calculated in Ref. [27], which is different from the MSP. The EM field can have an effect on the transport properties. The relative magnitudes of the components of the magnetization and the electric field depends on the frequency. Figure 2 shows the ratios ZH_y/E_z, ZH_x/E_z, at the interface as a function of the frequency, where Z is the free space wave impedance.

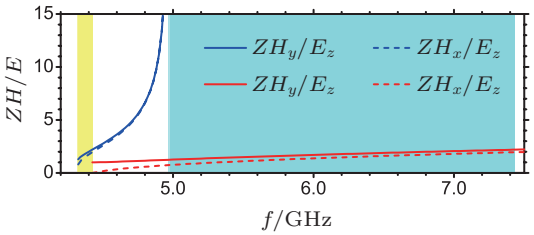


Fig. 2. The magnitudes of the components of the magnetic field along the wave vector (ZH_x) normalized by the electric field for the $k_z = 0$ MSP states as functions of the frequency f. Here Z is the free space wave impedance. The red line corresponds to the dispersion shows in Fig. 1; the blue line corresponds to the dispersion for a MSP mode moving in the opposite direction (not shown). The yellow and cyan regions in Fig. 1, denote two frequency ranges where MSPs propagate unidirectionally.

The MSP is completely described by its EM field, the information of the spin wave is implicitly included in the magnetic susceptibility. The interaction of the MSP and M can be formulated in terms of its EM fields.

2.2. MSP in a magnetic photonic crystal

Recently, there has been much interest in photonic crystals consisting of a periodic array of dielectric materials.[29–34] It is natural to consider a magnetic photonic crystal (MPC), which includes magnetic materials as one kind of its constituents. An external static magnetic field can affect the photonic band gaps (PBGs) of the MPC. As a typical tunable

PC, the MPC has attracted much interest[35–43] due to the fast switching time of magnetic systems.

We recently examined the photonic band of an MPC consisting of an array of ferrite rods[44] and found three different types of PBGs, which arise, respectively, from: (i) the multiple Bragg scattering; (ii) the Mie scattering resonance of individual ferrite cylinder de to the MSP; and (iii) the spin wave resonance. Not all of the PBGs are easily tunable, only those related to the MSP and the spinwave resonance can be easily manipulated. Most importantly the resonant types of PBG are robust against the position disorder of the magnetic scatterers. We will describe some typical examples of the photonic bands next.

We consider a MPC consisting of a two-dimensional (2D) array of ferrite rods. In this section, we focus on the 2D case with the wave vector perpendicular to the rods. In the 2D EM systems, the transverse electric (TE) mode and the transverse magnetic (TM) mode are independent eigenmodes and can be studied separately. For the TE (TM) mode, the magnetic (electric) field of the EM wave is polarized along z direction, parallel to the rods, The tunability works only for the TM mode.

The properties of the system can be described by the scattering phase shifts of the cylinders. By matching the tangential components of $\boldsymbol{E}$ and $\boldsymbol{H}$ at the boundary, the scattering phase shift η_n for the nth angular momentum channel (AMC)[45–48] can be obtained. The tangent of the scattering phase shift is found to be[44,49]

$$\tan\eta_n^H = -\frac{x_0\varepsilon_{\rm s}\mathrm{J}_n'(x_0) - x_2\mathrm{D}_n(x_2)\mathrm{J}_n(x_0)}{x_0\varepsilon_{\rm s}\mathrm{N}_n'(x_0) - x_2\mathrm{D}_n(x_2)\mathrm{N}_n(x_0)}, \tag{4}$$

for the H mode. Here $x_2 = k_2 r_{\rm s}$, $x_0 = k_0 r_{\rm s}$, $r_{\rm s}$ is the radius of the ferrite rod. $\mathrm{J}_n(x)$ and $\mathrm{N}_n(x)$ are Bessel and Neumann functions, respectively, and $\mathrm{D}_n(x) = \mathrm{J}_n'(x)/\mathrm{J}_n(x)$, η_n^H is independent of the sign of n. Similarly

$$\tan\eta_n^E = -\frac{x_1\mathrm{J}_n'(x_0) - x_0\varepsilon_{\rm s}\left[\zeta_n + \mathrm{D}_n(x_1)\right]\mathrm{J}_n(x_0)}{x_1\mathrm{N}_n'(x_0) - x_0\varepsilon_{\rm s}\left[\zeta_n + \mathrm{D}_n(x_1)\right]\mathrm{N}_n(x_0)}, \tag{5}$$

for the E mode, where $\zeta_n = nb/(x_1 d)$, and $x_1 = k_1 r_{\rm s}$. As can be seen, because $b \neq 0$, the phase shifts η_n^E for the nth and the $-n$th AMCs are different. Typical phase shifts for the lowest three angular momentum channels as a function of frequency are illustrated in Fig. 3. The scattering exhibits many resonances when the phase shift is equal to $\pi/2$.

Most photonic band structure calculations have been based on the plane-wave expansion method[50] or the finite difference time domain method.[51] However, for dispersive systems with gyromagnetic scatterers, it is rather difficult to achieve a reliable convergence of the solutions at frequencies near the scattering resonances. In particular, sometimes the plane wave expansion method may produce unreliable results.[52] For PCs consisting of non-overlapping spheres or circular cylinders, the multiple scattering method (MSM) proves to be the most powerful.[44,52–61] provided that the scattering matrix for individual scatterer can be obtained exactly. Thus, the multiple scattering method using the exact scattering matrix for 2D gyromagnetic rod[42–44,59–61] is employed in the photonic band structure calculation.

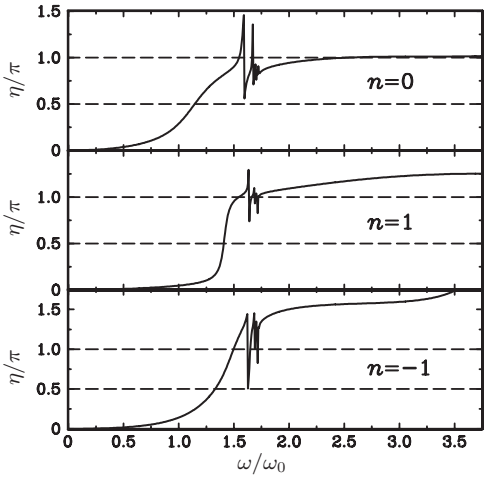


Fig. 3. Scattering phase shift of a ferrite cylinder as a function of the angular frequency normalized by the fmr angular frequency.

If the cylinder radius $r_{\rm s}$ is small enough so that $x_0 = k_0 r_{\rm s} \ll 1$, we obtain, for $n \neq 0$,

$$\tan\eta_n^E = \frac{\pi(k_0 r_{\rm s})^{2|n|}}{2^{2|n|}\,|n|!\,(|n|-1)!} \times \frac{d + b_{\rm s} - 1}{d + b_{\rm s} + 1}, \tag{6}$$

where $b_{\rm s} = nb/|n|$, $n \geq 1$.

A scattering resonance occurs when the tangent of the phase shift is infinite. The above formula suggests that at the angular frequency $\omega_{\rm h} = \omega_e + \omega_{\rm mag}/2$ when $d + b_{\rm s} + 1 = \mu_{\rm eff}^{-1} + 1 = 0$, an infinite number of scattering resonances occur for all $n > 0$, as $\tan\eta_n^E$ tends to infinity.[45]

In the long wavelength limit the tangent of the phase shifts for the H modes are given by

$$\tan\eta_n^H = \frac{\pi(k_0 r_{\rm s})^{2|n|}}{2^{2|n|}\,|n|!\,(|n|-1)!} \times \frac{1 - \varepsilon_{\rm s}}{1 + \varepsilon_{\rm s}}. \tag{7}$$

The resonance occurs for all n at the surface plasmon frequency with $\varepsilon_{\rm s} = -1$, as is well known. This degeneracy for the case when $\varepsilon \approx -1$ is termed multiple AMCs resonance.[46–48] This may lead to the superscattering of electromagnetic waves from a subwavelength scatterer[46–48] and, when a couple of resonant structures are put together, may exhibit spectral behavior similar to electromagnetically induced transparency (EIT).[62] For scattering off a sphere, the spherical Bessel functions are involved, scattering resonances for different AMC occur at different frequencies in the long wavelength limit[63,64] and no such degeneracy occurs.

We next examine the effect of these resonances in a MPC of periodically arranged cylinders. To study the magnetic effects we focus here on the E mode. In multiple scattering theory, the scattered field from a site i, $\boldsymbol{b}_i$, is related to the total

incoming field $\boldsymbol{f}_i$ by the scattering matrix of a single cylinder, t, in the form $\boldsymbol{b}_i = t\boldsymbol{f}_i$. The inverse single cylinder t matrix can be expressed in terms of the scattering phase shift η by $t_m^{-1} = 1 - i\cot\eta_m$. The total incoming field is a sum of the external incoming field $\boldsymbol{p}_i$ and the scattered waves from all the other scatters in the MPC slab, which can be written as: $\boldsymbol{f}_i = [\sum_{j\neq i} -\boldsymbol{S}_{ij}\boldsymbol{b}_j + \boldsymbol{p}_i]$. Here $\boldsymbol{S}_{ij}$ is a "structure factor" that transforms the outgoing wave from site j into an incoming wave at site i. The scattering amplitude $\boldsymbol{b}$ from the MPC slab is related to the amplitude $\boldsymbol{p}_i$ of the external wave by the full $\boldsymbol{T}$ matrix: $\boldsymbol{b}_i = \boldsymbol{T}\boldsymbol{p}_i$. From the above reasoning, we find that the inverse $\boldsymbol{T}$ matrix of the MPC slab is a sum of the single cylinder inverse t matrix and the structure factor $\boldsymbol{S}$

$$\boldsymbol{T}^{-1} = t^{-1} + \boldsymbol{S}. \tag{8}$$

The structure factor is determined from the geometry of the MPC slab and the scattering phase shift is determined from the susceptibilities of the cylinder. The matrix equation determining the photonic band structure can be written as

$$\boldsymbol{H}\boldsymbol{b} = 0, \tag{9}$$

where the real symmetric matrix

$$\boldsymbol{H}_{n,n'} = A(n-n') + \delta_{n,n'}\cot\eta_n^E. \tag{10}$$

The structure factor $A(n)$ is given by $A(n) = \mathrm{i}[S(n) + \delta_{n,0}]$, where the lattice sum[65] $S(n) = \sum_{\boldsymbol{R}\neq 0} \mathrm{i}^n \mathrm{H}_n^{(1)}(k_0 R)\,\mathrm{e}^{-\mathrm{i}\boldsymbol{k}\cdot\boldsymbol{R}}\,\mathrm{e}^{-\mathrm{i}n(\phi_{\boldsymbol{R}}-\phi_{\boldsymbol{k}})}$. $\mathrm{H}_n^{(1)}(x)$ is a Hankel function of the first kind. The summation runs over all lattice sites $\boldsymbol{R}$ except $\boldsymbol{R} = 0$, the wavevector $\boldsymbol{k}$ is in the first Brillouin zone (BZ); $\phi_{\boldsymbol{R}}$ and $\phi_{\boldsymbol{k}}$ are the azimuthal angles of $\boldsymbol{R}$ and $\boldsymbol{k}$, respectively.

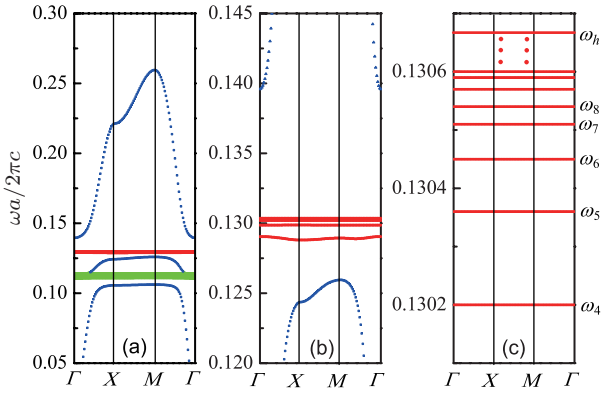


Fig. 4. Photonic band structure for a square lattice composed of ferrite rods of radius $r_s = 2$ mm and with the saturation magnetization $4\pi M_s = 1700$ gauss. The lattice spacing $a = 8$ mm. A magnetic field along z is applied such that $H_0 = 900$ Oe. The MSP bands are the flat bands shown in red in Fig. 1(a). (The green bands come from the spin waves. The regular Bloch bands are shown as black.) All of the flat bands lie below ω_h. On the expanded scale (b) and (c), the infinitely dense set of flat bands are illustrated.

Figure 4 shows the band structures for an MPC of a square lattice with lattice spacing $a = 8$ mm and rod radius $r_s = 2$ mm. Material parameters for the rods are taken from those for MgMn ferrites; namely, with the permittivity of the ferrite rod $\varepsilon_s = 12.6$, the saturation magnetization $4\pi M_s = 1700$ gauss. An external magnetic field is applied such that $H_0 = 900$ Oe. Accordingly, the magnetic surface plasmon resonance frequency is given by $\omega_h = \omega_e + \omega_{mag}/2 = 0.130667 \times (2\pi c/a) = 4.9 \times 2\pi$ GHz. In the band structure there are bands similar to that of an ordinary photonic crystal with photonic band gaps (PBG) due to the Bragg reflection. We denote these with blue lines. In addition, there are red MSP bands and the green spin wave bands. We found that the blue "Bragg" PBG scales with the inverse lattice spacing. This band gap changes very little when the external field is changed. The band structure near the red flat band region is shown on an expanded scale in Figs. 4(b) and 4(c). A dense set of flat bands is exhibited, whose number increases as one increases the cut-off angular momentum index n_c to include more AMCs in numerical calculation. Each flat band corresponds to resonances in a particular m-th AMC. In Fig. 4(b), we set $n_c = 5$, four flat bands are identified, corresponding to the resonance of the n-th AMC, with $n = 2, 3, 4$, and 5. Figure 4(c) shows the band structure with $n_c = 11$, there appear 10 flat bands [the flat bands corresponding to the resonances in the 2nd and 3rd AMC are not shown in Fig. 4(c) for clarity]. It is interesting to note that the frequency of the flat bands numerically satisfy a relation

$$\omega_n = \omega_3 + \frac{(n-3)(n+4)}{n(n+1)}(\omega_h - \omega_3),$$

for $n \geq 3$, with ω_3 dependent on material parameters ω_e and ω_{mag}, rod radius r_s, and the lattice spacing a.

The MSP frequency f_s, which depends on the external field through $\omega_0 = \gamma H_0$, determines the position of the spin wave (green) and the MSP (red) PBGs. We have plotted in Fig. 5 the photonic band structures for a hexagonal lattice for different external fields with the eigenfrequencies normalised by f_s. The location of frequency $f/f_s = 1$ corresponds to the top of the densely packed flat bands lying between the green and the red PBGs. This illustrates the effect of the external field in moving the frequency of the PBG through shifting the value of f_s. An increase of the external magnetic field makes the green and the red PBGs move upwards substantially.

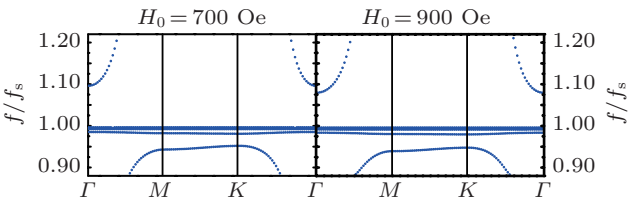


Fig. 5. The photonic band structures of a lattice of ferrite rods with frequency in units of the magnetic surface plasmon frequency f_s given by Eq. (3) for two values of the external field.

In the small r_s limit at frequencies near the single cylinder resonances, the red photonic band consists of a series of flat bands, as in Fig. 1(c). These bands occur at frequencies close to the MSP frequency f_s. This is why these are called the MSP bands. Their Chern numbers are equal to n mod N[18] where N is the degree of rotation symmetry of the crystal. We describe these next.

In the long wavelength limit the structure factor can be evaluated approximately near the BZ center by replacing the sum by an integral, yielding[66]

$$A(n) \approx \frac{4}{a^2(k^2-k_0^2)}\left(\frac{k}{k_0}\right)^{|n|}. \tag{11}$$

The off-diagonal element of $\boldsymbol{H}$, $A(n)$, is proportional to $(k/k_0)^{|n|}$ and vanishes faster than the diagonal elements as $\boldsymbol{k}$ approaches the BZ center. The band is thus determined by the vanishing of the diagonal term $A(0)+\cot\eta_n^E$. Since $\cot\eta_n^E$ as given by Eq. (6) is inversely proportional to $(k_0 r_s)^{2|n|}$ in the small r_s limit, the diagonal terms will not vanish unless $d+b_s+1=\mu_{\rm eff}^{-1}+1$ tends to zero. So equation (9) can be satisfied only if the frequency is close enough to the "Mie" scattering resonance frequency, so that $\mu_{\rm eff}+1\approx 0$. This determines the eigenfrequencies of the bands. The same argument also applies to the H modes with the eigenfrequencies close enough to the surface plasmon frequency so that $\varepsilon_s \approx -1$, as is previously found numerically. The case discussed here is thus the magnetic analog of the "surface plasmon" that was discussed previously. In two dimensions, according to Eq. (6) the scattering resonance occurs at a particular frequency ω_h for all AMCs with $n \geq 1$, As a result, close to the scattering resonance frequency, there will appear multiple numbers of eigenfrequencies (bands), each of which is dominated by a resonance in the m-th AMC, yielding $b_n = b_m\delta_{n,m}$. For the present case, due to the magnetic chirality, the resonance does not occur for both signs ($\pm m^{\rm th}$) of the AMC. This band structure is illustrated in Fig. 1. Numerical evaluation of $A(n)$ by direct summation and with the Ewald sum technique suggests that, for a crystal with p fold rotation symmetry, and for the higher angular momentum states, the factor $(k/k_0)^{|n|}$ in Eq. (11) is replaced by $(k/k_0)^m$ where

$$m = \mathrm{mod}\,(|n|, p). \tag{12}$$

For these bands, n is replaced by m.

We have computed the Chern numbers numerically for all of these flat bands, starting from $n=2$ up to $n=11$, based on a gauge-invariant numerical technique proposed in Refs. [67] and [68]. Our numerical calculations confirm the vanishing of the contribution to C_α from all $\boldsymbol{k}$ away from the BZ center, namely,

$$C_\alpha^{(|\boldsymbol{k}|>0)} = \frac{1}{2\pi \mathrm{i}}\iint_{|\boldsymbol{k}|>\varepsilon_{\boldsymbol{k}}} \mathrm{d}^2\boldsymbol{k}\,(\nabla_{\boldsymbol{k}}\times \boldsymbol{A}_{\alpha\boldsymbol{k}})\cdot\boldsymbol{e}_z = 0, \tag{13}$$

where ε_k takes an arbitrarily small positive value, namely, the surface integral is over the first BZ excluding $\boldsymbol{k}=0$. In addition, when applying the Stokes theorem to transform the surface integral over an area containing the BZ center into a closed path integral, the integration turns out to be independent of the path, provided that the path encloses the BZ center. This confirms that $\boldsymbol{A}_{\alpha\boldsymbol{k}}$ is singular only at the zone center.

3. Physical manifestation

3.1. Yin–Yang reflection (YYR) and nonreciprocal subwavelength optical devices

We first describe how an external electromagnetic field interacts with a MPC at frequencies close to the MSP frequency. Recently, there have appeared burgeoning activities in exploring the phenomena resulting from the time reversal symmetry breaking for photons. Among others, a skew scattering effect involving EM waves was discussed by Rikken and coworkers,[69] the EM one-way edge modes analogous to quantum Hall edge states were discussed by Haldane and Raghu,[70] and later by Wang and coworkers[71] in a magnetic photonic crystal system. An essential difference between the SP and the MSP is that the MSP is nonreciprocal, the magnetic system breaks time reversal symmetry. Thus, the bulk MSP dispersion described in Section 2.1 only exists for one direction of the wavevector. Even the tough magnetic photonic band described in Section 2.2 looks symmetrical, while the wave functions are not. We describe next how this is manifested.

A plane wave can be considered as a linear combination of waves with different angular momenta. For example, in two dimensions a plane wave of wave vector $\boldsymbol{k}$ can be expanded in terms of Bessel functions $\mathrm{J}_m(kr)$ as a sum of states of different angular momenta: $\exp(\mathrm{i}\boldsymbol{k}\cdot\boldsymbol{r}) = \sum_m \mathrm{i}^m \exp[\mathrm{i}m(\phi-\phi_k)]\mathrm{J}_m(kr)$. There are equal amounts of angular momenta components of opposite signs $\pm m$. When a plane electromagnetic (EM) wave is incident on a magnetic photonic crystal (MPC) consisting of a periodic array of magnetic cylinders, at some frequencies the reflected wave around a cylinder consists mostly of angular momenta of the same sign, while many angular momenta are suppressed. For example, the local reflected wave can consist mostly of the $n=0$ (s) and the $n=1$ (p) components and is well approximated by

$$-q_0\mathrm{H}_0(kr) - \mathrm{i}q_1\exp(\mathrm{i}\phi)\mathrm{H}_1(kr), \tag{14}$$

where q_0 and q_1 are constants. The reflected wave develops a "finite circulation". This "finite circulation" exhibits dramatic physical manifestations. When the sum of the wavelets from each cylinder is added up, the resulting reflected wave becomes proportional to

$$-\exp(-\mathrm{i}\boldsymbol{k}\cdot\boldsymbol{r})(q_0+\mathrm{i}q_1\,\mathrm{e}^{\mathrm{i}\phi_k}), \tag{15}$$

where $\boldsymbol{k}$ is the wave vector and ϕ_k is its orientation. As the direction of $\boldsymbol{k}$ is varied, the sign of $\exp(\mathrm{i}\phi_k)$ can change. The s and the p wave contribution can switch between destructive and constructive interference.

This is illustrated in Figs. 6 and 7, where we show the reflection of Gaussian beams of EM waves of opposite incoming directions from the MPC slab. In one direction, the reflected wave is very weak (Fig. 1) while in the other direction the intensity of the reflected wave remains substantial. In reflection, the tangential component of the $\boldsymbol{E}$ and the $\boldsymbol{H}$ fields are continuous. The circulation of the reflected wave is a manifestation of the photonic states inside the MPC. These photonic states occur at frequencies close to the scattering resonances of angular momenta of only one sign. This can occur at the analog of the surface plasmon for the magnetic degree of freedom. We will now describe our results in detail.

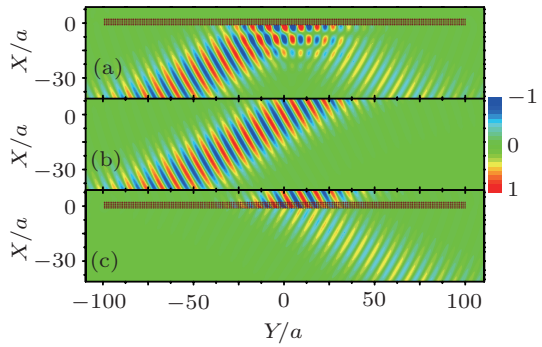


Fig. 6. The electric field pattern of (a) the total field, (b) the incoming field, and (c) the scattered field for a Gaussian beam incident from left hand side (incident angle $\theta_{\mathrm{inc}} = 60°$) upon a four-layer MPC slab. The electric field polarization of the Gaussian beam is along cylinder axis. The position of the ferrite rods are marked by the black dot.

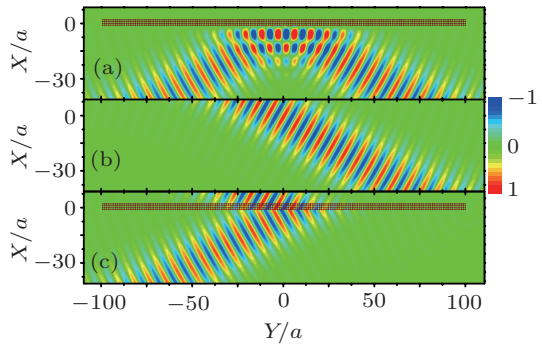


Fig. 7. The electric field pattern of (a) the total field, (b) the incoming field, and (c) the scattered field for a Gaussian beam incident from right hand side (incident angle $\theta_{\mathrm{inc}} = -60°$) upon a four-layer MPC slab. The electric field polarization of the Gaussian beam is along cylinder axis. The position of the ferrite rods are marked by the black dot.

Our results are obtained with the rigorous multiple scattering theory.[57–60] To clarify the physics, we show below a simple controlled analytic approximation and compare it with exact full-wave numerical calculations.

We have considered an example of a two-dimensional (2D) MPC composed of a square lattice (lattice constant $a =$ 8 mm) of ferrite cylinders of radius $r = 0.25\,a$ in air. The axis of the cylinder and the magnetization M_0 are along the z direction. In our numerical calculation, we have computed the matrix $\boldsymbol{T}$ by inverting the matrix $\boldsymbol{T}^{-1}$ for a finite four-layer MPC slab with each layer consisting of 200 ferrite rods. The scattering amplitudes are obtained by multiplying $\boldsymbol{T}$ and $\boldsymbol{p}$. In this paper we focus on the polarizations with the electric (E mode) field parallel to the cylinder axis.

We have considered numerical examples of incoming Gaussian beams with angles of incidence of $\pm 60°$. The beam center is focused on the middle (100-th) ferrite rod in the first layer. The working frequency is selected as $f_w = 4.84$ GHz, located near to the MSP frequency

$$f_{\mathrm{s}} = \frac{1}{2\pi}\left(\omega_0 + \frac{1}{2}\omega_m\right) = 4.9\ \mathrm{GHz}.$$

The results are shown in Figs. 6 and 7. It is evident that there exists a remarkable difference for the reflected Gaussian beams at different directions. To gain a deeper understanding of our results, we show the corresponding angular momenta components $|b_i^m|$ at the sites of different cylinders i of the MPC slab in Figs. 8 and 9. As advertised, only the angular momentum components of positive m (0 and 1) are dominant. There is a difference in magnitude for the opposite incoming directions. The scattering fields are only large in the first layer and do not penetrate into the MPC slab. This provides a simple way to obtain a controlled analytic approximation for the scattered fields.

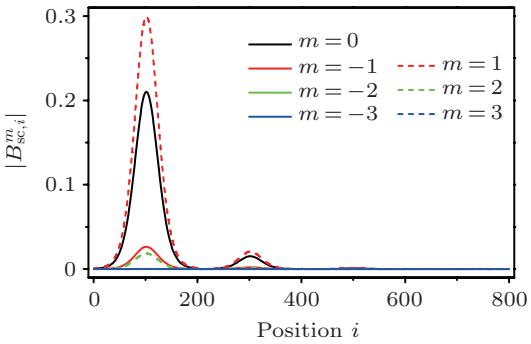


Fig. 8. The scattering amplitude for different angular momenta components at different positions for an incoming angle of 60°. Labels 1–200, 201–400, 401–600, and 601–800 correspond to the first, second, third, and fourth layers.

As we mentioned, the total incoming field at a site i, $\boldsymbol{f}_i$, is a sum of the external incoming field $\boldsymbol{p}_i$ and the scattered waves from other scatters of the MPC slab: $\boldsymbol{f}_i = \sum_{j\neq i} \boldsymbol{S}_{ij}\boldsymbol{b}_j + \boldsymbol{p}_i$. Because the scattered fields $\boldsymbol{b}_j$ are only significant in the first layer, in the sum over j we can restrict our attention to terms j only in the topmost first layer. The reflection problem for the 2D MPC can be well approximated by the reflection problem from the one-dimensional (1D) MPC consisting of the topmost layer. As usual, we consider an incoming plane wave, so there is a translational invariance along this layer. The eigenstates are characterized by a wave vector k_y. The 1D $\boldsymbol{T}$ matrix is

diagonal in k_y, its inverse involves the coupling between angular momentum states and is given by $\boldsymbol{T}^{-1} = [t^{-1} + \boldsymbol{S}]$ with $\boldsymbol{S}(m) = \sum_{Y\neq 0} \exp(\mathrm{i}k_y Y)\mathrm{H}_m(k_0 Y)\exp(\mathrm{i}m\phi_Y)$.

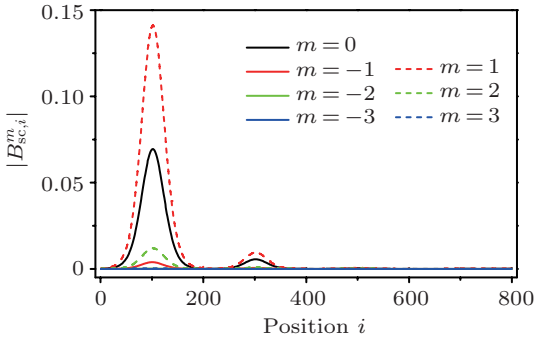


Fig. 9. The scattering amplitude for different angular momenta components at different positions for an incoming angle of $-60°$. Labels 1–200, 201–400, 401–600, and 601–800 correspond to the first, second, third, and fourth layers.

Near the MSP bands, only a few angular momentum states are important, the inversion of $\boldsymbol{T}^{-1}$ is simple. More precisely, at this frequency range only a few scattering phase shifts are close to the resonance, so that $\cot\eta_m$ is small. For most other m's $\cot\eta_m$ is large. Accordingly, $t_m^{-1} = 1 - \mathrm{i}\cot\eta_m$ is usually small only for a few positive m. The inversion of $\boldsymbol{T}^{-1}$ can be analytically carried out. For the example considered here, only the $m = 0$ and $m = 1$ phase shifts are significant. $\boldsymbol{T}^{-1}$ is then approximated by a 2×2 matrix, which can be easily inverted. More precisely, with $a_m = t_m^{-1} + \boldsymbol{S}(0)$ and $x = \boldsymbol{S}(1)$, we obtain

$$\boldsymbol{T} = \begin{bmatrix} a_1 & -x \\ x & a_0 \end{bmatrix} / (a_0 a_1 + x^2), \quad \boldsymbol{p} = \begin{bmatrix} p_1 \\ p_0 \end{bmatrix}, \tag{16a}$$

$$\begin{bmatrix} b_1 \\ b_0 \end{bmatrix} = \begin{bmatrix} a_0 p_1 - x p_0 \\ a_1 p_0 + x p_1 \end{bmatrix} / \det, \tag{16b}$$

where $\det = (a_0 a_1 + x^2)$.

Since $\exp(-\mathrm{i}\mathbf{k_i}\cdot\mathbf{r}) = \sum_n (-i)^n \exp[in(\phi - \phi_{ki})]\mathrm{J}_n(k_i r)$, $p_n = (-i)^n (k_{ix} - \mathrm{i}k_{iy})^n / k_i^n$. The magnitude of angular momentum components of the scattered field obtained with Eq. (2) for plane wave is shown in Fig. 10 as a function of the angle of incidence. This is in good agreement with our detailed numerical results, which are also shown in Fig. 10. We have performed calculations for incident plane wave and Gaussian beams. For the whole range of incident angles, the results obtained for plane waves and Gaussian beam are almost the same. It can be seen that there exists a distinct asymmetry for the scattering amplitude of the positive and negative incident angles because of the finite circulation around the ferrite rods.

We have also considered the frequency dependence of our effect. As the frequency is increased, one moves away from the resonance; the $m = 1$ scattering phase shift is decreased. In Fig. 11 we show the angular momentum components for an incoming wave of frequency $f = 9.5$ GHz. As can be seen, the $m = 0$ component is now much bigger than the $m = 1$ component and the $m = 1$ component is almost the same as $m = -1$ component, which means that the circulation around the ferrite rod is small. The consequence from this is that the scattered amplitude for the positive and negative angle are almost the same. Accordingly, the curve of scattering amplitude versus the incident angle is nearly symmetric.

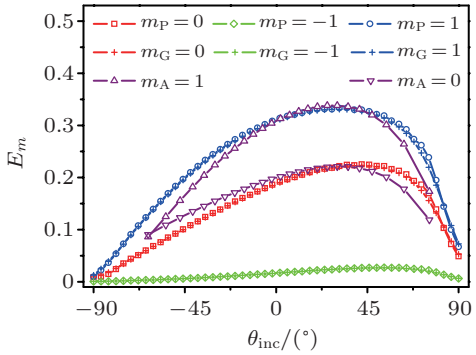


Fig. 10. Numerical results for the magnitude of angular momentum components of the scattered field E_0, E_{-1}, and E_1 for plane waves (subscript P), Gaussian beams (subscript G) as a function of the incident angle (lines) and analytic results (subscript A) obtained with Eq. (17). The operating frequency is at $f = 4.8$ GHz.

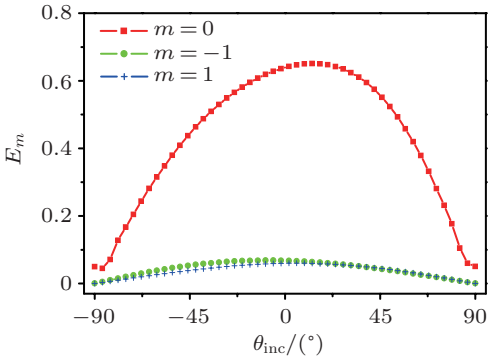


Fig. 11. The magnitude of angular momentum components of the scattered field E_0, E_{-1}, and E_1 obtained with simplified multiple scattering formula as a function of the incident angle. The operating frequency is at twice the MSP frequency, $f = 9.5$ GHz.

We next examine the physical meaning of the electric field. The electric field at position $\boldsymbol{r}$ scattered from the collection of cylinders at positions $\boldsymbol{r}'_j$ is given by $E = -\sum_j \mathrm{e}^{-\mathrm{i}k_y y'_j}[q_0 \mathrm{H}_0(k_0 R) - q_1 \mathrm{H}_1(k_0 R)(X + iY)/R]$, where $R = |\boldsymbol{r}'_j - \boldsymbol{r}|$, $X = x'_j - x$, and $Y = y'_j - y$. Equation (5) can be written as $E = -2\exp(-\mathrm{i}k_y y)\sum_{y'_j>0}\cos(k_y Y)[q_0 \mathrm{H}_0(k_0 R) - q_1 \mathrm{H}_1(k_0 R)X/R] - \sin(k_y Y) q_1 \mathrm{H}_1(k_0 R) Y/R$. We focus on the far field when the sums can be replaced by integrals and obtain

$$E \approx -2\exp(-\mathrm{i}k_x x - \mathrm{i}k_y y)[q_0 \pm \mathrm{i}q_1 \exp(\pm \mathrm{i}\phi_k)]/|k_x|a, \tag{17}$$

where the $+$ $(-)$ sign is for negative (positive) X. The above equation explicitly shows that the magnitude of the reflected wave depends on q_0, q_1 and ϕ_k, which in turn are functions of the incoming direction and thus depend on the sign of k_y, as is demonstrated in Figs. 10 and 11.

The nonreciprocal character is further illustrated in the reflection of an EM wave due to a line source from a slab of a square lattice of YIG rods.[75–79] This is shown in Fig. 12, where the incoming wave is due to a line source near the surface radiating at a frequency near the MSP resonance frequency f_s. The lattice constant is $a = 8$ mm and the radius of YIG rod $r = a/4$. We focus on the transverse magnetic (TM) wave with the electric field polarized along the rod axis. In this case, the working frequency of the line source is $f = 5$ GHz, located $1.0a$ away from a four-layer MM slab. The applied external static magnetic field is such that $H_0 = 900$ Oe, corresponding to a MSP resonance frequency $f_s = 4.97$ GHz. The electric field pattern and the x-component of the Poynting vector are shown in Figs. 12(a) and 12(b), respectively. The reflected EM wave can be drastically molded, such that the field appears dramatically different on opposite sides of the source. On the left hand side the reflected wave substantially attenuates the incoming field, giving rise to a darkened region near the surface of the MM, while on the right hand side the scattered field enhances the incoming wave, resulting in a brightened region.

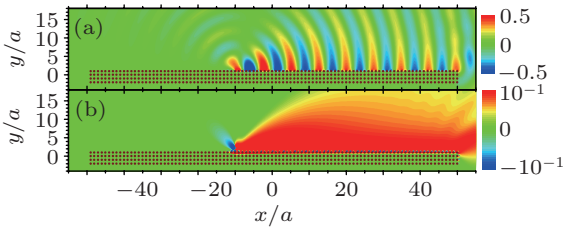


Fig. 12. The electric field pattern (a) and the x-component of the Poynting vector (b) for a line source located near the surface of an MM slab. The working frequency of the line source is $f = 5$ GHz, close to the MSP resonance. The lattice spacing $a = 8$ mm and the radius of the ferrite rod $r = 2$ mm. The reflection is drastically molded.

Near the MSP resonance, because of the broken time reversal symmetry, the the angular momenta content of the scattered wave off a magnetic cylinder are mainly of one sign, with the other sign almost completely suppressed. A giant circulation of energy flow develops,[75–79] so only the energy flow in one direction is supported, as shown in Fig., 12(b) where the rightward energy flow is sustained and reinforced, while the leftward energy flow is substantially suppressed. Consequently, the phenomenon originates from the combined action of MSP resonance and TRS breaking. The working frequency of YYR can be controlled by tuning the MSP resonance frequency f_s with an external magnetic field. This makes the YYR effect more favorable in the design of EM devices.

The above effect can be used in designing a straight one-way waveguide. As is discussed in the previous section, in the vicinity of MSP resonance frequency there exist photonic gaps,[44] so that the EM wave can be confined between two MM slabs, similar to the conventional photonic crystal waveguide. In our design the magnetization of two MM slabs are in opposite directions, such that the EM wave reflected forward from one MM slab will also be reflected forward from the other, leading to a different design of a one-way EM waveguide from those in Refs. [70]–[74], as is illustrated in Fig. 13(a) where a line source is placed at $(-5.5a, 0)$, between two MM slabs $2a$ apart. The parameters for the MM slabs and the operating frequency of the line source are the same as in Fig. 12. It can be seen that the EM wave propagates rightward, in the left hand side it is completely suppressed. To further demonstrate the one-way characteristic, we display in Fig. 13(e) the rightward transmitted power, $T_x = \int_{-3a}^{3a} P_x \mathrm{d}y$, as a function of x, which suggests that the energy transfers rightward with $T_x > 0$. In addition, the EM energy only experiences an extremely low decay rate of less than 0.1 dB/λ when considering realistic material parameters for YIG ferrite.

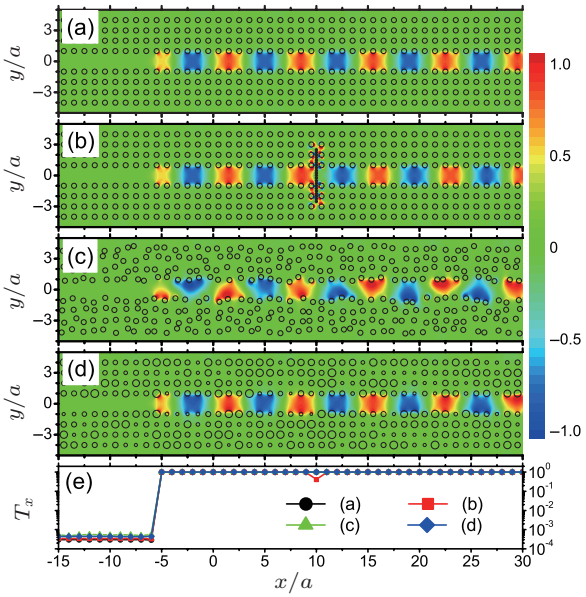


Fig. 13. The design of a straight unidirectional waveguide with two MM slabs of opposite magnetization and $2a$ apart. Numerical simulations of the electric field pattern for a line source placed in the channel indicate one-way transportation of EM wave in the configurations (a) without defect and disorder, (b) with PEC defect, (c) with position disorder, and (d) with radius disorder. The working frequency is $f = 5$ GHz. Panel (e) displays the normalized transmitted power versus x for (a), (b), (c), and (d). The open circles denote the YIG rods while the solid circles in panel (b) indicate the PEC defect.

We have also considered the robustness of the design against defect and disorder as shown in Figs. 13(b)–13(d). Figure 13(b) corresponds to the electric field pattern when a PEC defect of about $2\lambda/3$ is inserted into the channel. The EM wave is seen to circumvent the PEC defect, maintaining almost complete power transmission along the channel, as shown in Fig. 13(e). This indicates that the leftward backscattering wave from the defect is completely suppressed and, therefore, the wave gets around the defect and keeps moving rightward. By comparing with the defect free waveguide shown in Fig. 13(a), it can be found that the defect changes only the phase of the rightward propagating wave, which is a

result of the delay due to the defect. In Figs. 13(c) and 13(d), we present, respectively, the electric field patterns for the cases when position and radius disorders of the YIG rods are introduced. To be specific, the position disorder is introduced by allowing the coordinates of each rod to vary with a maximum displacement equal to $a/4$ while the radius disorder permits r to fluctuate up to 50% of the unperturbed radius. As can be seen, the disorder only has an influence on the wave patterns, but not the power transmission. It should be noted that for the edge state waveguide,[70–74] the working frequency lies in the Bragg type of photonic gap, so, although the system can be immune to the defect, it may suffer from disorder of the building blocks. The above effects have been observed experimentally.[75,80–83] They can also be used to define efficient beam benders and splitters,[75–79] which we will describe next.

The results for the electric field distribution in our design of a one way waveguide together with a beam splitter on top are shown in Fig. 14. The line source is located at $(0, -15a)$. The channel width is equal to 0.27 times the wavelength. If one reverses the orientation of the magnetization for those rods with coordinates $x < 0$ in the horizontal MPC, the EM wave will split, as shown in Fig. 14(b). The wave experiences an extremely low reflection at the corner, as can be seen from Fig. 14(c). The results in the deep subwavelength regime, as well as the effects of different kinds of defects, are discussed in Ref. [1] and will not be repeated here.

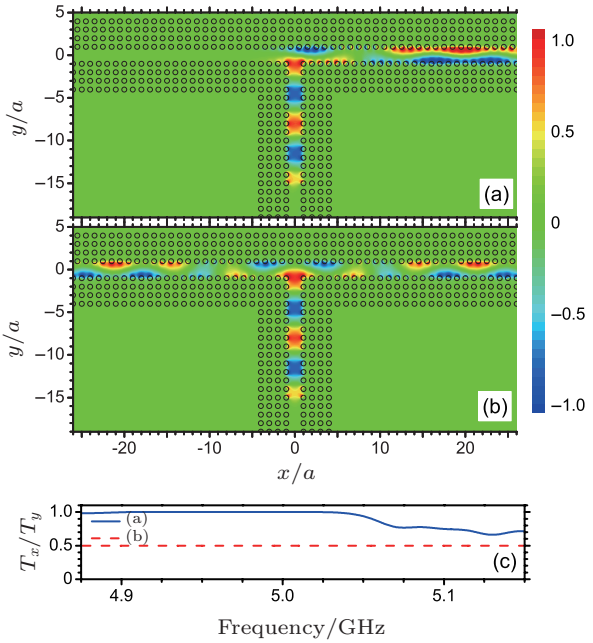


Fig. 14. The electric field patterns showing a vertical one way waveguide with a 90° bend (a) and a splitter (b); curves in panel (c) corresponds the transmissivity T_x/T_y versus frequency, where $T_x = \int_{-3a}^{3a} P_x \mathrm{d}y$ denotes the rightward transmitted power in the right wing and $T_y = \int_{-3a}^{3a} P_y \mathrm{d}x$ the upward power in vertical channel.

We have carried out a numerical demonstration of the coupling to this waveguide, as shown in Fig., 15 where we present the electric field patterns when a Gaussian beam is incident along an interconnect/waveguide with the width of the channel equal to $4a$. There is an impedance mismatch, so that the field inside is less than that outside. Once inside, the Gaussian beam can pass the channel for one direction, while for the opposite direction it is completely suppressed. One-way waveguides have recently been proposed using "edge" states localized near the interface of two claddings. Our design does not rely on these localized states since the damping coefficient α in the present case is twenty times larger. If the surface states play the role, then the EM field will be heavily damped, which is not the case shown in Fig. 15. Furthermore, the size of the surface states is less than a, while the channel width $4a$ here is much larger than the combined size of the top and bottom surface states. Consequently, one-way forward scattering based on MSP resonance is the essential mechanism.

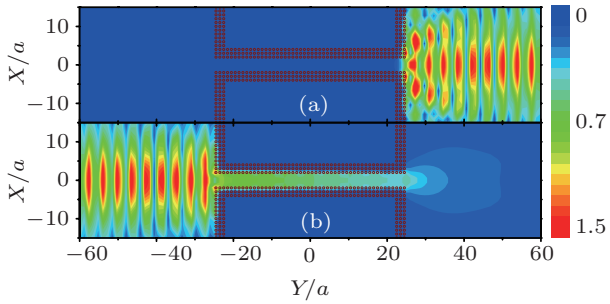


Fig. 15. The electric field patterns when a Gaussian beam is incident along the channel with the width of the channel equal to $4a$. The Gaussian beam can pass the channel for one direction, while for the opposite direction it is completely suppressed.

In conclusion, we have studied the reflection of EM waves from MPCs. The reflected wave is found to exhibit a strong circulation at frequencies so that the scattering of some angular momentum states of one sign is close to the resonance condition. An example of this corresponds to the surface plasmon bands. Magnetic surface resonances also occur at frequencies close to the spin wave band[44] and we expect our calculation to be applicable to that case as well. The physics around this region will be discussed in Section 2.3.

3.2. Electrical detection of the MSP

Spintronics, which provides a promising way to overcome the limitation of charged-based electronics in data storage and processing, have received enormous attention recently.[84,85] A crucial process in spintronics is the injection of spin and charge currents between structures, at least one of which is magnetic. The injection current is reduced when there is an impedance mismatch across the junction. Improving the injection efficiency is of the utmost importance. The injection can be local, as in vertical structures, or nonlocal, as in planar structures. Nonlocal structures hold the promise for large scale integrated circuits applications. Current nonlocal spin transfer

structures[86–89] exploit diffusive spin currents. In this structure, the distance traveled by the signal is equal to the spin diffusion length l_{sf}, and is of the order of 1000 Å. Recently, the focus of spin injection in vertical structures has shifted to structures involving magnetic insulators, such as yttrium iron garnet (YIG),[20–22] where the loss may be smaller.

The exploitation of magnetic surface plasmons (MSPs) in spintronics has not been discussed previously but the MSPs offer many intriguing potentials. MSPs on bulk insulating magnetic surfaces are also known as Damon–Esbach[13] magnetostatic modes. They are coupled modes of the surface spin wave and the electromagnetic (EM) wave and are the magnetic analog of the better known (electric) surface plasmons. These states differ from bulk spin waves in that the frequency of these states are in the band gap region and corresponds to nonpropagating bulk spin waves. They differ from surface plasmons in that they are nonreciprocal because of the broken time reversal symmetry of magnetic systems. This leads to the absence of backscattering, which is also exhibited by electronic "edge" states in the quantized Hall effect[14] and in topological insulators.[91] Stimulated by recent focus on plasmonics, there has been interest in MSPs that can be generated on the surface of magnetic insulators, such as YIG.[75–79]

When an EM wave falls on a metal, it is strongly reflected due to the high impedance mismatch; very little signature of this wave is left in the metal. A surface plasmon has an EM wave component and thus is also completely reflected when it strikes a metal. In plasmonics, the injection of surface plasmons into metals has never been considered. Whereas a surface plasmon is nearly totally reflected, a MSP incident on a metal is absorbed now that the reflected surface wave is inhibited by the broken time reversal symmetry.

Stimulated by a desire to improve upon the spin injection efficiency, to reduce the loss of the signal over distance of nonlocal structures, by recent interests in spin wave logic devices[92,93] and by experimental results of voltage generation in a metal film M on YIG under microwave excitation,[94] we have recently studied the injection of an MSP into M (which may or may not be ferromagnetic), as is illustrated in Fig. 16. We found that the MSP can be efficiently injected into M by the incoming electric and magnetic field regardless of the interface "impedance mismatch", generating a static voltage due to the Hall effect in the metal and also a spin current if M is a ferromagnet. This provides for the electrical detection of the MSP. In addition, since the transport of the MSP is ballistic, the loss of the signal over propagating distance is much reduced. The distance travelled by the MSP is macroscopic, of the order of a centimeter. It is larger than the spin diffusion length of current nonlocal spin valve structures by five orders of magnitude. Finally, due to the partial spin wave nature of the excitation, the MSP can be easily coupled to spin wave logic devices and provides an efficient connection between different circuit elements. We will now describe our results in detail.

The nonlocal geometry we have in mind is illustrated in Fig. 16. Magnetic surface plasmons can be generated at the surface of a magnetic insulator with an external oscillating RF field, such as from a strip line, away from a finite metallic element M deposited on the surface of a magnetic insulator. In the following we shall illustrate our ideas with parameters such that the magnetic insulator is YIG. The geometry in Fig. 16 is very similar to that of recent experiments,[20–22] the results of which are interpreted in terms of bulk spin waves with no restriction on the direction of the wave vector. In the present case, the frequency is in the gap region of the long wavelength bulk spin wave. The wave vector can only go in one direction. The effect will be changed when the YIG magnetization is reversed.

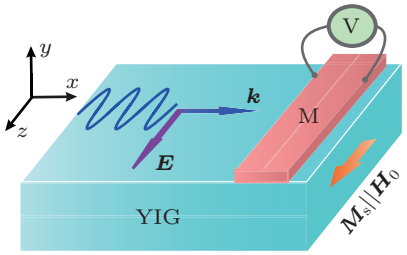


Fig. 16. Schematic diagram of the geometry for the injection of an MSP into a metallic element M. The MSP has wave vector $\boldsymbol{k}$ along x and the electric field $\boldsymbol{E}$ parallel to the magnetization $\boldsymbol{M}_s$.

We next discuss the interaction of the MSP with the metallic film. The usual formulation of spin and charge injection focuses on the matching of the spin and charge current at an interface. In the present case there are no charge currents; the boundary occurs in air and there are no discontinuity in the magnetic properties in the YIG substrate. An MSP is a mixture of a spin wave and an EM wave localised near the interface. The MSP is completely described by its EM field, the information of the spin wave is implicitly included in the magnetic susceptibility. The interaction of the MSP and M can thus be formulated in terms of its EM fields.

Usually, when an EM field strikes a metal, it is strongly reflected. This is what happens with the electric surface plasmon. For the MSP, there are no states with negative k_xs that it can be reflected to. We have considered the possibility that the MSP is stopped at the interface, then goes along the edges of M and around it. This will involve states with finite k_z and with $k_x = 0$. We find that states with $k_z \neq 0$ are not possible. This can be seen from the following physical argument. For a nonzero k_z, the transverse electric (TE) and the transverse magnetic (TM) modes are coupled; the EM wave in YIG have a finite component of the electric field E_y in the direction perpendicular to the film. A finite E_y induces electric charges at

the interface and implies that the state will also have an electric surface plasmon character. This is not possible unless one of the dielectric constants is negative.

We have also considered the possibility of the wave going up at the air–M boundary. To this end we have studied states at the air–YIG interface localized near M with imaginary in plane (along x) wave vectors but real wave vectors in the direction perpendicular to the interface (along y). We found that there are no states going up from the air–YIG interface. The only states possible are those coming in from above. Thus, there are no surface states for the incoming MSP to escape to, and this state can be injected into M. In the following, to illustrate our result, we consider the case with the MSP wave vector perpendicular to the direction of the magnetization ($k_z = 0$). The electric field is then along z. The tangential electric and magnetic fields E_z, H_y, and the perpendicular field B_x inside M, are the same as that of the incoming MSP because there are no reflected waves. We denote quantities in M and YIG with superscripts M and Y; the quantities in air have no superscripts. The tangential electric field inside M, $E_z^{\rm M}$, generates a current with current density given by $\boldsymbol{J}^{\rm M} = \sigma \boldsymbol{E}^{\rm M}$ where σ is the conductivity. The electric field is a sum of the external field $\boldsymbol{E}$ and that due to the Hall effect: $\boldsymbol{E}^{\rm M} = R_{\rm H}\boldsymbol{J}^{\rm M} \times B + \boldsymbol{E}$. From these two equations, which are linear in $\boldsymbol{J}^{\rm M}$, we can solve for $\boldsymbol{J}^{\rm M}$ in terms of $\boldsymbol{E}$. In the present geometry, only E_z is not zero. We obtain

$$\mathrm{J}_z^{\rm M} = \sigma E_z/(1 + R_{\rm H}^2\sigma^2 B^2).$$

This current along z generate an electric field along x of magnitude

$$E_x^{\rm H} = -R_{\rm H}^{\rm M} B_y^{\rm M} \mathrm{J}_z^{\rm M}, \tag{18}$$

where $R_{\rm H}^{\rm M} \approx -1/(ne)$ (n is the density of the electrons) is the Hall coefficient of M, and the superscript H denotes the E field due to Hall effect. As we emphasized at the beginning of this paper, the fields only depend on the intrinsic properties of the metal and are not functions of the interface properties and any possible "impedance mismatch". The product of $E_z^{\rm M}$ and $B_y^{\rm M}$ and, hence, $E_x^{\rm H}$ possess finite time independent components. In general M has no electrical leads attached to it and is in an open circuit situation. Charges will be induced at the surface until an electric field of magnitude $\langle E_x^{\rm H}\rangle$ is developed and the current stops flowing. This corresponds to a voltage $U_x = \int_0^{L_x} \mathrm{d}x \langle E_x^{\rm H}\rangle$ where L_x is the length of M in the x direction. The total voltage is controlled by the spatial dependence of the EM wave inside M. We show next that the electric field decays in M with a length scale of the order of an effective skin depth.

The electric field in a medium is described by Maxwell's equation $\Omega E(r) = 0$ where $\Omega = \boldsymbol{\nabla} \times \mu^{-1}/\varepsilon \boldsymbol{\nabla} \times -\omega^2$; μ is the magnetic permeability; ε is the dielectric constant. Here we have used units so that the speed of light $c = 1$. In principle, the electric field inside M/YIG can be calculated from its value at the boundary with a Green's function technique[75] from the equation

$$\begin{aligned} E(r) \;=\; & -\int \mathrm{d}S \cdot [(\mu^{-1}/\varepsilon \nabla \times E(r_{\rm S})) \times G(r, r_{\rm S})^* \\ & - (\mu^{-1}/\varepsilon \nabla \times G(r, r_{\rm S}))^* \times E(r_{\rm S})], \end{aligned} \tag{19}$$

where the surface integral is carried out at the YIG-air YIG-M boundary, G is the Green's function defined by: $\Omega' G(r, r') = \delta(r' - r)$. The operator $\Omega' = \Omega_{\rm M}$ for $y > 0$, $\Omega' = \Omega_{\rm YIG}$ for $y < 0$, G can be constructed from a linear combination of products of photonic states including the M–YIG MSP states as $G = \sum_{k_x} |n\rangle\langle n|/(k_0^2 - \omega_n^2(k_x))$ where ω_n, $|n\rangle$ are the eigenvalues and the eigenstates of Ω'. The Green's function is dominated by contributions from the MSP states at the air–M–YIG interface with energy $\omega_n(k_x) = k_0^2$ when the denominator is zero. Thus, the spatial dependence will be determined by these states, which we will study next. To illustrate the physics, we first consider the simpler case where the thickness of M is larger than the spatial extent of the MSP. The MSP state at the air-YIG interface is coupled to the MSP state at the M–YIG interface, which can be constructed as follows.

MSP for M/YIG The properties of the interface MSP state is obtained by matching $\mathrm{H}_{\parallel}$ and $B_{\perp}$ of the plane wave states of YIG and that in M. We obtain the dispersion for the YIG–M MSP state given by

$$k_{x\rm M}^2 \approx -\omega^2 \varepsilon_{\rm M}/[(b' - b + a)^2/a' - a']. \tag{20}$$

Here $a = \mu_{x,x}^{-1}(\mathrm{YIG})$, $b = \mu_{x,y}^{-1}(\mathrm{YIG})$; $a' = \mu_{x,x}^{-1}(\mathrm{M})$, $b' = \mu_{x,y}^{-1}(\mathrm{M})$. ε, $\varepsilon_{\rm M}$, are the dielectric constant of YIG and M. These states can be excited by the incoming MSP and decays exponentially with a length scale of the order of inverse skin depth $1/\kappa = 1/\mathrm{Im}[(\omega\varepsilon_{\rm M}/a')^{1/2}]$ away from the air/YIG–M/YIG boundary.

MSP for a trilayer structure So far we have assumed that the thickness of M is larger than the spatial extent d_y of the MSP, d_y is of the order of a mm. Current experiments are carried out with the thickness t of the metallic film of the order of nm and much less than d_y. It is necessary to take the finite thickness of M into account.

We have calculated the interface states in the air/M/YIG trilayer structure by matching the boundary EM fields at both the air/M and the M/YIG interfaces. We found that in the limit when $t \ll 1/\kappa$, k_x as given by Eq. (20) is modified so that $\varepsilon_{\rm M}$ is replaced by an effective dielectric constant that is reduced by an amount of the order of $t\kappa$. Furthermore, the real and the imaginary parts of k_x are opposite in sign. In place of Eq. (20) the dispersion is now given by

$$k_{x\rm M}/[\omega^2 \varepsilon_{\rm M} t] \approx -1/(1 + a + b); 1/(1 + a - b).$$

The two solutions have opposite signs for the real part of k_x. The voltage generated is determined by the imaginary part of the wave vector and is given by

$$U_x = R_{\rm h}\sigma B_y E_z \min(l, L_x), \tag{21}$$

where $l^{-1} \approx 2\omega^2 \,{\rm Im}[\varepsilon_{\rm M}]t/(1+a-b)$ is of the order $t\kappa^2$. For $t \approx 10$ nm and a skin depth κ^{-1} of the order of a micron, we obtain $l \approx 0.1$ mm. We next estimate the magnitude of this effect.

We take M to be Au with a Hall coefficient $R_{\rm H} = 7.25 \times 10^{-11}$ m^3/C, and a conductivity $\sigma = 4.55 \times 10^7/(\Omega\cdot{\rm m})$. Thus $E_x^{\rm H} = 3.3 \times 10^{-3} B_y E_z$. We estimate the product BE from the power P of the input coplanar waveguide. We assume that most of the power is expanded in generating the MSP. The energy current

$$S = {\rm EB}/\mu_0 = P/A, \tag{22}$$

where A is the area of the wave. For current experimental systems, the width in the z direction is of the order of a mm; the y extent of the MSP is also of the order of a mm. Thus, $A \approx 1$ mm^2. We obtain $\langle E_z B_y\rangle \approx 4\pi Pc/(10 v_{\rm MSP})$. Using the above estimate of l and for P of the order of a watt, U_x is of the order of a micro-volt.

Most metals are paramagnets. Because of YIG, or in the presence of an external magnetic field, the electrons in M have a small magnetization. A nonferromagnetic metal usually does not possess local moments at all atomic sites and we do not expect exchange coupling between the YIG spins and this small magnetization in the paramagnet. The electric field E_z generates an AC current inside M. As the electric field oscillates from parallel to opposite the direction of the induced magnetization, a residual DC current can also be generated if the resistances along the two directions are different. This can happen if there is a significant amount of spin orbit impurity scattering. The resistance along the two directions will then be different, resulting in a net average current/voltage in this transverse direction. We next consider a situation where the metal is a ferromagnet.

The Hall coefficient $R_{\rm H}$ of ferromagnets contains a component due to the anomalous Hall effect and the magnitude of the above effect can be modified. In ferromagnets, a spin current is also induced. At the air/YIG–M/YIG boundary, the perpendicular component of the magnetic field B_x and the tangential component H_y are continuous. Whereas the magnetization density in air is zero, there is a finite change in the x, y components of the magnetization density at the boundary inside the ferromagnet. We can obtain the magnetization density from the equation $\boldsymbol{M}(M) = [\boldsymbol{B}(M)/\mu_0 - \boldsymbol{H}(M)]$, $M_{x,y}$ act as sources to create magnetization currents in the ferromagnet.

From these we get the magnetization current given by $\boldsymbol{J}_M = {\rm i}\omega \boldsymbol{M}$ with

$$M_x = (a' - 1/\mu_0 - b'^2/a')B_x + {\rm i}b'B_y/(\mu_0 a'), \tag{23}$$

$$M_y = \left\{B_y[1 - 1/(\mu_0 a')] - {\rm i}b'B_x/a'\right\}/\mu_0. \tag{24}$$

Associated with the change in $M_{x,y}$ there is a static change in the longitudinal magnetization M_z to second order: $\Delta M_z = \sqrt{M_0^2 - M_x^2 - M_y^2} - M_0 \approx -(M_x^2 + M_y^2)/(2M_0)$. This induces an additional charge current given by[95,96] $\boldsymbol{J}' = -D_{\rm M}\nabla(\Delta M_z)$ where $D_{\rm M}$ is the diffusion constant that relates the charge current to the longitudinal magnetization change. In the open circuit situation, this provides for an additional contribution to the DC potential given by[97]

$$U = \int \boldsymbol{J}'/\sigma \approx D_{\rm M}\langle M_x^2 + M_y^2\rangle/(2M_0\sigma). \tag{25}$$

Here, the angular bracket refers to the time average of the transverse magnetization squared. We next estimate the magnitude of U as a function of frequency.

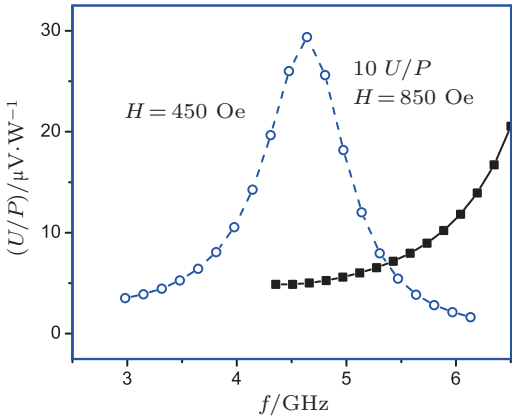


Fig. 17. The output voltage from the spin current normalized by the incoming power as a function of frequency for the higher frequency branch of the MSP for external magnetic fields $H_{\rm ext} = 450$ Oe (dotted line) and $H_{\rm ext} = 850$ Oe (solid line).

The ratio $D_{\rm M}/\sigma$ is of the order of $1/(N(E_{\rm F})\mu_{\rm B}e)$ where $N(E_{\rm F})$ is the density of states at the Fermi surface; μ_B, the Bohr magneton; and e is the electric charge. From Eq. (22) we get $\langle B_y^2\rangle = P\mu_0/(v_{\rm MSP}A)$. We take M to be permalloy with a density of states $N(E_{\rm F}) \approx 3 \times 10^{28}/({\rm ev/m}^3)$. For the spin wave parameters, we have found recently[98] that the fmr frequency of thin permalloy film as a function of frequency and external field $H_{\rm ext}$ can be fitted by the typical spin wave formula $f_{\rm sw}$ with saturation magnetization $\mu_0 M_0 = 1$ T, and total field $H_0 = H_{\rm ext} - 126.6$ Oe. Our estimates for the voltage U normalized by the incoming power P as a function of frequency for the upper branch of the MSP are shown in Fig. 17 for external fields of magnitudes 850 Oe and 450 Oe. The results for $H_{\rm ext} = 850$ Oe are multiplied by a factor of 10. As can be seen, the magnitude of this contribution is of the order of microvolts. It can exhibit a peak as a function of frequency. This peak is due to the fmr resonance of the permalloy metallic film when a' is close to zero. The magnitude of this peak

depends on the Gilbert damping parameter, which we have set to a value of 0.03.

It is likely that the spins of YIG and that of the ferromagnet are exchange coupled. The continuity of H_x and B_y across the YIG–ferromagnet interface imposes partial alignment of the spins between these two materials. Spin currents in the FM will also generate some residual spin wave in YIG. In the present calculation, the exchange coupling between spins can be incorporated in the magnetic susceptibility in Eq. (1) by including the exchange energy in f_0.

In conclusion, we study the nonlocal spin and charge current generation in a finite metallic element on the surface of magnetic insulators with the magnetic surface plasmon (MSP), which is absorbed and cannot be reflected. The MSP generates a voltage in the longitudinal direction that is proportional to the power. If the metal is a ferromagnet, then a spin current can also be generated in the longitudinal direction. Our results will be useful for new classes of devices using spin waves.

3.3. Entangled transverse optical vortex

Over the last thirty years there has been much interest in physical states that are topological in nature because they are not destroyed by local perturbations. An example of this state is the vortex, which exists not only in fluids but also in optics.[99–101] The optical vortex has found many different interesting potential applications,[102–112] including multiplexing and encoding[113,114] at optical frequencies. This photonic vortex state, which exhibits an orbital angular momenta parallel to the beam direction, is generated with a spatial light modulator using liquid crystals with a low switching time (milliseconds). In this section,[115] we discuss a new kind of photonic states with finite angular momenta perpendicular to the beam direction, the transverse optical vortex (TOV). The TOV provides for an extremely simple and fast (Gb/s) way to digitally encode and decode information in a microwave. Because the TOV signal depends on the sign of the vorticity, which is topological in nature, the encoded information is unaffected by the endemic problem of fluctuations in intensity (fading) in microwave communications. We will now discuss our results in detail.

Encoding The TOV states can be generated from the reflection of a microwave from a magnetic photonic crystal (MPC), which consists of an array of ferrite rods with a thickness that can be as thin as 1/15 to 1/20 of a wavelength, as is illustrated in Fig. 18. We have found that at frequencies close to the ferromagnetic resonance (spin wave) frequency, the reflected field is a linear combination of states of finite transverse vorticities of the same sign. The sign of the vorticity can be changed by a reversal of the direction of the external field and takes a nanosecond, which is much faster than the response time of liquid crystals.

Our results are obtained with the rigorous multiple scattering theory carried out with detailed numerical and simple analytic calculations. In the multiple scattering theory, the scattering field from a site i can be expressed as a sum of othronormal basis functions with coefficients $\boldsymbol{b}_{\mathrm{sc},i}$. Our work is motivated by recent interest in the broken time reversal symmetry in magnetic systems. This results in an asymmetric scattering of light from magnetic cylinders between angular momentum channels m and $-m$.[75–79] The scattering amplitude $\boldsymbol{b}_{\mathrm{sc}}$ from a photonic crystal is related to the amplitude $\boldsymbol{p}_i$ of the external wave by the full $\boldsymbol{T}$ matrix

$$\boldsymbol{b}_{\mathrm{sc},i} = \boldsymbol{T}\boldsymbol{p}_i. \tag{26}$$

Our result is obtained by computing $\boldsymbol{T}$ and, hence, $\boldsymbol{b}_{\mathrm{sc},i}$.

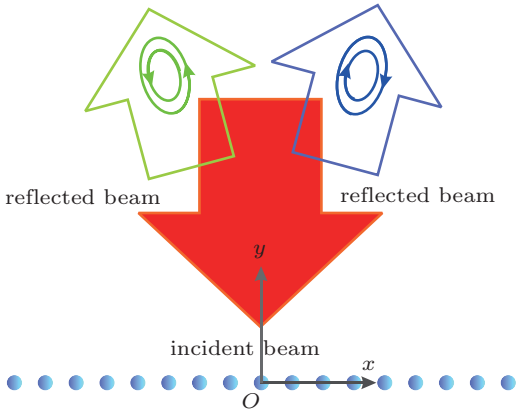


Fig. 18. Schematic diagram of the geometry of the problem. The beam is at normal incidence on an array of ferrite rods. At some frequency, the reflected beam carries a transverse vorticity perpendicular to the beam propagation direction. The sign of these effects can be switched (from blue to green or vice versa) within a timescale of nanoseconds when the external magnetic field is reversed, rendering another potential degree of freedom for data transmission as orbital angular momentum in the optical vortex, with an advantage of robustness and high speed generation.

We have considered an example of a single layer of ferrite cylinders of radius $r = 0.25a$ and lattice constant $a = 8$ mm in air arranged uniformly along the x direction. The axis of the cylinder and the magnetization M_0 are along the z direction. The magnetic susceptibility tensor is of a typical resonance form.[24] We have considered both a finite lattice as well as an infinite lattice. In the first case, the calculation is carried out numerically. In the second case, there is translational invariance along this layer. The eigenstates are characterized by a wave vector k_x. The $\boldsymbol{T}$ matrix is diagonal in k_x. The results from the two approaches are indistinguishable when the number of rods is larger than 300. Our analytic calculations are carried out for different k_x, which is conserved. To illustrate our result, we pick the most dramatic case with the direction of the EM wave coming in along the y direction perpendicular ($k_x = 0$) to the thinnest possible slab of a single layer of array of ferrite rods. The EM wave is uniform along z. Our

result for the scattered wave of different angular momenta m, $|b_m(k_x = 0)|$, normalized by the incoming wave as a function of the dimensionless frequency fc/a is shown in Fig. 19. Only b_0, b_1 are significant. This comes from the scattering resonances of the $m = 0$ and the $m = 1$ channels, b_{-1} is small. Because of the nature of the magnetic material, there is no scattering resonance for the $m = -1$ channel and $b_m \neq b_{-m}$; the average vorticity is finite. As the external field is reversed, the average vorticity is changed; b_{-1} and b_0 become much bigger than b_1. By summing over the scattered wave from all of the sites i, the reflected wave is obtained. We will discuss this next.

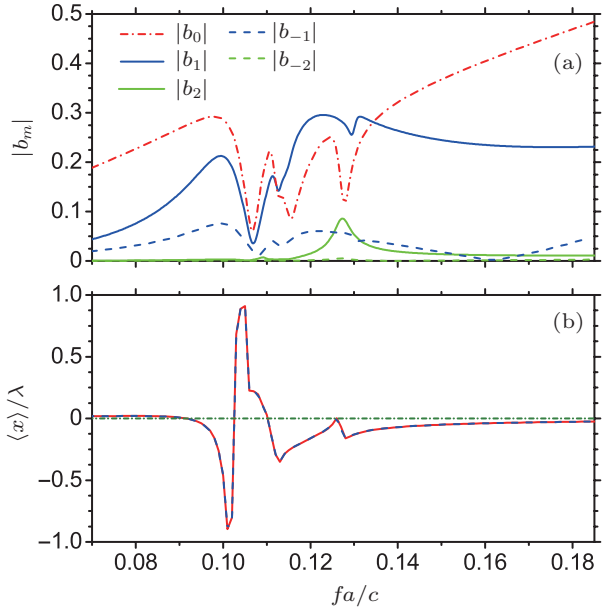


Fig. 19. (a) The magnitude $|b_m|$ of the scattering coefficients of different angular momentum channels m's (upper panel) and (b) the lateral shift $\langle x\rangle$ of beam center at $y = 2\lambda$ (lower panel) as a function of frequency.

The total scattered wave f_{0k} can be obtained by summing up the contributions from each of the partial waves of different angular momenta scattered from each of the cylinders. For the scattered wave, the x component of the wave vector can differ from that of the incoming wave by a reciprocal lattice vector $G_j = 2\pi j/a$: $k_{jx} = k_x + G_j$. The corresponding y wavevector for the reflected wave is given by $k_{jy} = (k^2 - k_{jx}^2)^{1/2}$.

We have found that

$$f_{0k} = \sum_j \exp[\mathrm{i}(\boldsymbol{k}_j \cdot r)]h_{k_j}, \tag{27}$$

where

$$h_k = -2\sum_m b_m \exp(\mathrm{i}m\phi_k)/(\mathrm{i}^m k_y a),$$

and $\phi_k = \tan^{-1} k_y/k_x$ measures the orientation of the wave vector $\boldsymbol{k}$, h_k is a sum of terms of different vorticities m. Because $b_m \neq b_{-m}$, a finite vorticity is developed. In previous studies of optical vortices,[99–101] the electric field has a Fourier component proportional to $\exp[\mathrm{i}m\phi_{k_\perp}]$ where $k_\perp$ is the component of k in the xz plane perpendicular to the direction of propagation. In our case, the angle ϕ_k is in the longitudinal plane, the vortex is transverse.

Decoding We envision that a TOV wave packet is generated via reflection, as is described above. This packet is sent out through space as a parallel beam with a telescope, which is then received by another telescope and focused as a beam onto the focal plane, as is illustrated in Fig. 20. We consider a receiver consisting of an array of dielectric rods. The decoding is illustrated schematically in Fig. 21. For this encoded beam coming in at normal incidence, the reflected beam goes away from the normal with a finite average velocity parallel to the surface that is in opposite directions for opposite signs of the TOV. We will explain this next.

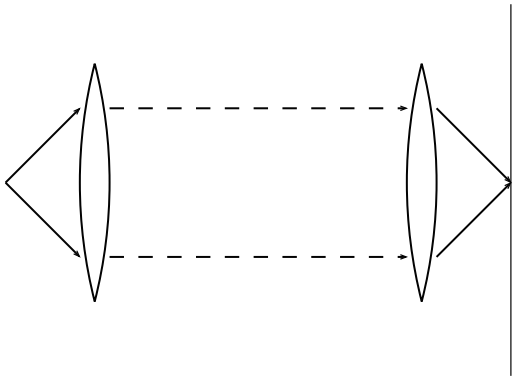


Fig. 20. Schematic diagram of the free space data transfer via the TOV state. A pulse is encoded on the left, converted to a parallel beam, sent to a receiver, reconstituted and decoded by a receiver on the right.

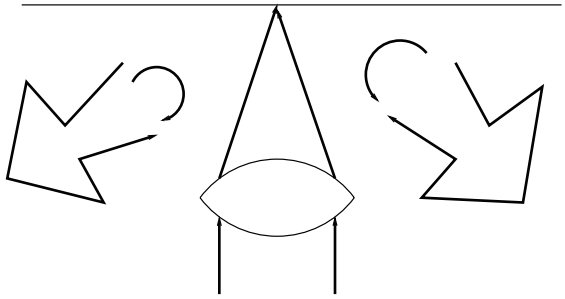


Fig. 21. Schematic diagram of the decoding of the TOV. The beam is focused by a telescope at normal incidence on a focal plane that consists of an array of dielectric rods. The reflected beam is off the normal direction and goes in opposite transverse direction for opposite signs of the TOV.

When the TOV state is converted to a parallel beam by the outgoing lens, the phase memory is retained and this phase depends on its distance from the lens center. When this parallel beam is reconstituted at the receiver, a TOV wave packet is recovered. For simplicity, we model the focused beam to be of Gaussian shape with the electric field polarized along the cylinder axis, with a spatial distribution given by

$$E_i(x) = (2/\pi)^{1/4} w^{-1/2} \exp(-x^2/w^2); \tag{28}$$

at the focal plane ($y = 0$) so that $\int \mathrm{d}x|E|^2 = 1$. The typical widths w that we have considered are of the order of 2 to

4 times the wavelength. We denote the Fourier transform of $E_i(x)$ by $\tilde{E}_i(k)$.

For each of the Fourier components, similar to Eq. (1) the scattered wave from a dielectric cylinder is given by

$$\boldsymbol{b}'_{\rm sc} = \boldsymbol{T}_{\rm d}\boldsymbol{p}', \tag{29}$$

where $\boldsymbol{T}_{\rm d}$ is the $\boldsymbol{T}$ matrix of the dielectric cylinder. The incoming wave is a TOV state: $p'_m \propto b_m \neq p'_{-m}$. As a result, for the scattered wave $b'_m \neq b'_{-m}$. Again similar to Eq. (2), the total reflected wave from the "receiving" dielectric cylinders is given by

$$f'_k = \sum_j \exp[{\rm i}(\boldsymbol{k}_j \cdot r)]h'_{k_j}, \tag{30}$$

where $h'_k = -2\sum_m b'_m \exp({\rm i}m\phi_k)/({\rm i}^m k_y a)$. This is of the same functional form as the original TOV state. For an incoming Guassian wave packet, the reflected wave is given by the sum over the different Fourier components

$$E^s(r) = \sum_k f(k)\exp({\rm i}\boldsymbol{k}\cdot r)/(2\pi). \tag{31}$$

An unusual aspect of the TOV photonic wave packet is a finite average Poynting vector in the direction perpendicular to the mean beam direction, which is given by

$$P_x = \langle k_x\rangle/k_0. \tag{32}$$

From Eq. (31), we obtain $P_x = {\rm Re}\int {\rm d}k_x k_x |f'_k\tilde{E}_i(k)|^2/k_0$. If a single angular momentum channel m dominates, then we get $P_x = \int {\rm d}k_x k_x |b'_m\tilde{E}_i(k)/(2ak_y)|^2$. This is odd in k_x and equals to zero at perpendicular incidence. On the other hand, if two channels, such as the $m=0$ and the $m=1$ angular momentum channels, are important, then we get a contribution $P_x = {\rm Re}\int {\rm d}k_x k_x^2 {\rm i}(b'_0 b'^*_1 - b'^*_0 b'_1)/k|E_0(k)/(2ak_y)|^2$, which is even in k_x and is not equal to zero. For the state with an opposite TOV consisting of the $m=0$ and the $m=-1$ channels, the sign of $\langle P_x\rangle$ is reversed. Thus, the reflected beam will go in different directions for different signs of the transverse vorticity.

Because the optical force contains a contribution from the Poynting vector,[116,117] when a particle is placed in the beam it will experience a net transverse force. Another way to decode the TOV state is to examine its effect on a particle. To provide for a further confirmation and a deeper physical understanding of this phenomenon, we will describe next an approximate analytic evaluation of the integral in Eq. (6).

Using the saddle point method, we have found that

$$E^{\rm s}(x,y) \propto h_{k_{\rm s}}\exp[-0.5(x-x')^2/(w^2/2+{\rm i}y/k)+{\rm i}ky], \tag{33}$$

where the Gaussian beam appears to be shifted by the amount

$$x' = \sum mb'_m/{\rm i}^m\exp({\rm i}m\phi_{k_{\rm s}})/[k\sum b'_{\rm m}/{\rm i}^m\exp({\rm i}m\phi_{k_{\rm s}})]; \tag{34}$$

where $k_{\rm s}$ is determined from the equation $k_{{\rm s},x} = {\rm i}(x-x')/(w^2/2+{\rm i}y/k)$.

If a single scattering channel at angular momentum m dominates, then we obtain a real shift with $x' = -mk_y/k^2$. For our example, both the $m=0$ and $m=1$ scattering channels are important, we obtain

$$x' \approx -{\rm i}k_y b'_1\exp({\rm i}\phi_{k_{\rm s}})/[k^2(b'_0 - {\rm i}b'_1\exp({\rm i}\phi_{k_{\rm s}})].$$

Now x' contains an imaginary part which contributes to the velocity. The expression for the electric field has an imaginary phase factor equal to ${\rm i}\boldsymbol{v}\cdot r = px+ky$ where the effective velocity $\boldsymbol{v} = (p,k)$ with

$$p = -{\rm Im}(x')/(w^2/2+{\rm i}y/k).$$

Thus the velocity has a x component, providing further confirmation of our claim of a finite $\langle P_x\rangle$. Just as for $\langle P_x\rangle$, this transverse velocity comes from an "interference" effect between the two angular momentum channels.

A finite transverse velocity implies that, for a wave packet the average position $\langle x\rangle = \int {\rm d}x x|E(r)|^2$ will change as the wave packet moves away from the surface. We thus turn our attention to $\langle x\rangle$. In the lower panel of Fig. 2 we show our numerical result for the average position of a typical TOV for the original reflected wave packet at the ferrite rods source normalized by the wavelength, $\langle x\rangle/\lambda$, as a function of the frequency of the incoming wave. For the ferrite, there are two frequencies that are of interest,[44] the spin wave frequency $\omega_{\rm SW} = \sqrt{\omega_0(\omega_0+\omega_m)} = 0.727c/a$ ($f_{\rm SW}a/c = 0.1157$) and a so-called magnetic surface plasmon (MSP) frequency $\omega_{\rm MSP} = \omega_0 + \omega_m/2 = 0.8359c/a$. As can be seen from Fig. 2 the shift $\langle x\rangle$ becomes significant and shows a dramatic dependence on the frequency in the region around the spin wave frequency. The Goos–Hanchen (GH) effect[118] predicts a shift in position of a reflected wave. In the GH effect, the displacement is zero at perpendicular incidence. Furthermore, the GH effect predicts that the shift at an angle is proportional to the film thickness, up to the skin depth. Our film is of thickness of 1/20 of a wavelength. Yet, $\langle x\rangle/\lambda$ is significant. All of these are different from the predictions of the GH effect.

The transverse displacement is a function of the distance away from the interface. This is shown in Fig. 5 for different frequencies. The position of the wave packet in the top panel is extracted from the mean position of the beam at different distances from the ferrite rods, the shapes of which are shown in the two lower panels in the same figure.

The two curves for the top panel of Fig. 22 shows that the sign of the velocity changes when the frequency changes by only 5%. We have considered different widths of the Gaussian beam w. The results are qualitatively the same. For the remainder of this paper we describe the angular momentum carried by the TOV.

The z component of the angular momentum, $L_z = (x\partial_y - y\partial_x)/\mathrm{i}$ of this state can be easily evaluated. We obtain $\langle L_z\rangle = \int \mathrm{d}\boldsymbol{r}E^{\mathrm{s}*}(r)L_zE^{\mathrm{s}}(r) = \int \mathrm{d}\boldsymbol{k}f_k^*(\partial_{\phi_k}/\mathrm{i})f_k$. Thus

$$\langle L_z\rangle \propto \sum_m m|b_m|^2 / \sum_m |b_m|^2. \tag{35}$$

Because $b_m \neq b_{-m}$, there is a net angular momentum, as is advertised.

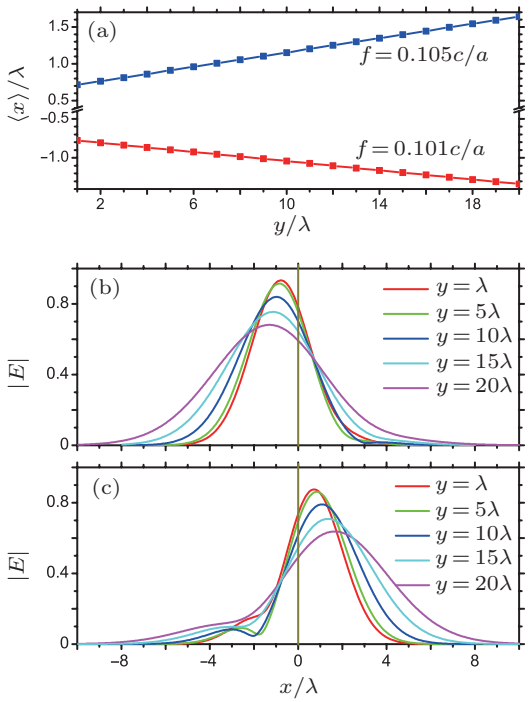


Fig. 22. (a) The beam center $\langle x\rangle$, as a function of the distance y from the array; $w = 2\lambda$, $r_s = 0.25a$. (b) and (c) Pulse shape at different distances y for $fa/c = 0.101$ and $fa/c = 0.105$, respectively.

In conclusion, we discuss the generation of a "transverse optical vortex" (TOV) in a microwave from the reflection from an array of ferrite rods under an external magnetic field. For this TOV state, the orbital angular momentum is perpendicular to the beam direction. This TOV state provides for a simple way to transfer digital information through space with the time separation between bits of the order of a nanosecond.

4. Perspective

The topic of this review is a confluence of three currently very active areas and has not been much studied. There is much promise of discovering new physics in this new virgin territory. The area of plasmonics was motivated by the surfaced enhanced Raman scattering and the enhanced transmission through subwavelength holes in a metallic film, which is capturing increasing interest due to their different promising applications, such as for subwavelength transport of electromagnetic (EM) wave.[3] These phenomena are associated with the interaction of EM waves and the surface plasmon. Because of the symmetry of Maxwell's equations with respect to its magnetic and electric degrees of freedom, there is a magnetic analog to the (electric) surface plasmon (SP), which on bulk surfaces is known as the Damon–Esbach mode. We have found the term magnetic surface plasmon (MSP) is more suggestive and more general. These states are "one-way". The MSPs also go in only one direction and can be considered as an optical analog of the electronic edge state in the quantized Hall effect. The MSP in a magnetic photonic crystal form a dense set of bands and exhibits increasing Chern numbers modulo the degree of rotation symmetry of the crystal.[18] These provide for a system to study the physics of higher-order topological invariants, which usually requires near degenerate bands with different Chern numbers.

The MSP has the potential to become a key player in spintronics. Spintronics is focused on the spin polarized transport of electrons and has a broad economic impact with the potential of providing new devices. The transport properties of a system can be changed and tuned with little time delay by a small external magnetic field. For example, in the magnetoresistance of a multilayer system, the magnetization of alternating layers can be switched by a small external field and the transport properties of the system are changed substantially. Because of the advances in nanotechnology, different small magnetic structures can be realized and studied. The MSP can be injected into a metallic element and generate spin and charge currents. Thus, it is coupled to the spin polarized transport of electrons. Its physical properties can be easily tuned by an external magnetic field.

Appendix A: Recapitulation of ordinary surface plasmon

Take the surface normal along y. We denote physical quantities on opposite sides of the interface with a subscript $i = 1, 2$. The wave vector parallel to the interface, $k_\parallel$, is the same on both sides. From $\nabla \cdot \boldsymbol{D} = 0$, we obtain

$$k_\parallel \boldsymbol{D}_{\parallel i} + k_{yi}\boldsymbol{D}_{yi} = 0. \tag{A1}$$

Now $\boldsymbol{D}_y$ and $E_\parallel$ are continuous; thus the ratio $\boldsymbol{D}_{yi}/E_{\parallel i}$ is also continuous

$$\boldsymbol{D}_{y1}/E_{\parallel 1} = \boldsymbol{D}_{y2}/E_{\parallel 2}. \tag{A2}$$

We thus obtain $k_\parallel \varepsilon_i/k_{y1} = -\boldsymbol{D}_y/E_\parallel = k_\parallel \varepsilon_2/k_{y2}$. For the surface state, k_{yi} is of opposite signs on opposite sides of the interface. We thus obtain

$$|k_{y1}|/\varepsilon_1 + |k_{y2}|/\varepsilon_2 = 0. \tag{A3}$$

For the SP to be stable, and for this equation to have a solution, the dielectric constant on opposite sides of the equation are opposite in sign to each other. The above equations do not involve the magnetic susceptibility and remain true even

for magnetic systems. For nonchiral systems, we also have $k_{\|}^2 + k_{yi}^2 = \varepsilon_i \mu_i \omega^2$. Dividing by ε_i^2 and subtracting from each other, we obtain

$$k_{\|}^2 (1/\varepsilon_1 + 1/\varepsilon_2) = \omega^2.$$

This is the dispersion for surface plasmons that is often quoted.

Appendix B: MSP (Damon–Esbach)

We now consider the magnetic analog of the above. We take the magnetization along z and the surface normal along y. We consider the case with $k_z = 0$ and denote the wavevectors and the $\boldsymbol{B}$ fields in YIG as $(k_x, k_y, 0)$, (B_x, B_y, B_z); in air, $(k_x, q_y, 0)$, (b_x, B_y, B_z). The inverse magnetic susceptibility tensor is denoted by

$$\mu^{-1} = \begin{bmatrix} a & -\mathrm{i}b & 0 \\ \mathrm{i}b & a & 0 \\ 0 & 0 & 1 \end{bmatrix}.$$

From Maxwell's equation, the dispersions of the electromagnetic wave in air and in YIG are given by

$$k_x^2 + q_y^2 = \omega^2/c^2 = k_0^2,$$
$$\omega^2 \varepsilon = (k_x^2 + k_y^2) a,$$

respectively.

Similar to Eq. (A1), $\boldsymbol{B}$ is perpendicular to the wavevector. We assume a spatial dependence of the form $\exp(\mathrm{i}\boldsymbol{k}\cdot x)$ and obtain

$$k_x B_x + k_y B_y = 0, \tag{B1}$$
$$k_x b_x + q_y B_y = 0. \tag{B2}$$

Similar to Eq. (A2), H_x and B_y and, hence, H_x/B_y are continuous. We obtain the relation

$$k_y a = q_y + \mathrm{i}bk_x. \tag{B3}$$

For localized states, the wave vectors $k_y = \mathrm{i}k_y'$, $q_y = -\mathrm{i}q_y'$ are imaginary. If $b = 0$, then this equation is completely analogous to Eq. (A3). The broken time reversal symmetry of magnetic systems is manifested in a finite b.

$$k_z \neq 0.$$

We next consider the MSP with $k_z \neq 0$ and show that this is not possible unless one of the dielectric constants is negative. From Maxwell's equation, we get $-\omega \boldsymbol{D}_y/c = (k_z H_x - k_x H_z)$. When $k_z = 0$ and $H_z = 0$, $\boldsymbol{D}_y = 0$. Now $H_x = \mu_{xx}^{-1} B_x + \mu_{xy}^{-1} B_y \neq 0$. Thus, when $k_z \neq 0$, $\boldsymbol{D}_y \neq 0$. The electric field of the MSP state possesses a component perpendicular to the interface and thus will also have an (electric) surface plasmon character. Equations (A1)–(A3), remain applicable to the present case. Equation (A3) cannot be satisfied unless one of the dielectric constants is negative.

References

[1] Ebbesen T W, Lezec H J, Ghaemi H F, Thio T and Wolff P A 1998 *Nature* **391** 667
[2] Barnes W L, Dereux A and Ebbesen T W 2003 *Nature* **424** 824
[3] Zayats A V, Smolyaninov I I and Maradudin A A 2005 *Phys. Rep.* **408** 131
[4] Atwater H A 2007 *Sci. Am.* **296** 56
[5] García de Abajo F J 2007 *Rev. Mod. Phys.* **79** 1267
[6] Maier S A 2007 *Plasmonics: Fundamental and Applications* (New York: Springer)
[7] Wu W, Bonakdar A and Mohseni H 2010 *Appl. Phys. Lett.* **96** 161107
[8] Zhang C, Chang H T, Zhao F Y and Hu X H 2013 *Opt. Lett.* **38** 4037
[9] Couture M, Zhao S S and Masson J F 2013 *Phys. Chem. Chem. Phys.* **15** 11190
[10] Homola J 2008 *Chem. Rev.* **108** 462
[11] Fleischmann M, Hendra P J and McQuillan A J 1974 *Chem. Phys. Lett.* **26** 163
[12] Lombardi J R and Birke R L 2008 *J. Phys. Chem. C* **112** 5605
[13] Damon R W and Eshbach J R 1961 *J. Phys. Chem. Solid* **19** 308
[14] Halperin B I 1982 *Phys. Rev. B* **25** 2185
[15] Simon B 1983 *Phys. Rev. Lett.* **51** 2167
[16] Kohmoto M 1985 *Ann. Phys.* **160** 355
[17] Hatsugai Y 1993 *Phys. Rev. Lett.* **71** 3697
[18] Chui S T, Liu S Y and Lin Z F 2013 *Phys. Rev. E* **88** 031201
[19] Chui S T, Lin Z F, Xiao J Q and Chang C R 2013 *J. Appl. Phys.* **113** 233910
[20] Heinrich B, Burrowes C, Montoya E, Kardasz B, Girt E, Song Y Y, Sun Y Y and Wu M Z 2011 *Phys. Rev. Lett.* **107** 066604
[21] Burrowes C, Heinrich B, Kardasz B, Montoya E A, Girt E, Sun Y, Song Y Y and Wu M Z 2012 *Appl. Phys. Lett.* **100** 092403
[22] Sandweg C W, Kajiwara Y, Chumak A V, Serga A A, Vasyuchka V I, Jungfleisch M B, Saitoh E and Hillebrands B 2011 *Phys. Rev. Lett.* **106** 216601
[23] Sandweg C W, Kajiwara Y, Ando K, Saitoh E and Hillebrands B 2010 *Appl. Phys. Lett.* **97** 252504
[24] Slichter C P 1978 *Principle of Magnetic Resonance* (Berlin: Springer-Verlag)
[25] Pozar D M 2005 *Microwave Engineering* (3rd edn.) (New York: Wiley)
[26] Wohfarth E P 1986 *Ferromagnetic Materials* (Amsterdam: North-Holland)
[27] Xiao J and Bauer G E W 2012 *Phys. Rev. Lett.* **108** 217204
[28] Kittel C 1963 *Quantum Theory of Solids* (Eq. (97) in page 66) (New York: Wiley)
[29] Yablonovitch E 1987 *Phys. Rev. Lett.* **58** 2059
[30] John S 1987 *Phys. Rev. Lett.* **58** 2486
[31] Joannopoulos J D, Meade R D and Winn J N 1995 *Photonic Crystals* (Princeton: Princeton University Press)
[32] Joannopoulos J D, Johnson S G, Winn J N and Meade R D 2008 *Photonic Crystals* (2nd edn.) (Princeton: Princeton University Press)
[33] Soukoulis C M 1993 *Photonic Band Gaps and Localization* (New York: Plenum)
[34] Soukoulis C M 1996 *Photonic Band Gap Materials* (Dordrecht: Klumer)
[35] Sigalas M M, Soukoulis C M, Biswas R and Ho K M 1997 *Phys. Rev. B* **56** 959
[36] Nagesh E D V, Subramanian V, Sivasubramanian V and Murthy V R K 2006 *Physica B* **382** 45
[37] Lyubchanskii I L, Dadoenkova N N, Lyubchanskii M I, Shapovalov E A and Rasing Th 2003 *J. Phys. D* **36** R277
[38] Jia W L, Li Y Z, Xi Y G, Jiang P, Xu X H, Liu X H, Fu R T and Zi J 2003 *J. Phys.: Condens. Matter* **15** 6731
[39] Inoue M, Fujikawa M R, Baryshev R A, Khanikaev A, Lim P B, Uchida1 H, Aktsipetrov O, Fedyanin A, Murzina T and Granovsky A 2006 *J. Phys D* **39** R151
[40] Xu J, Wu R X, Chen P and Shi Y 2007 *J. Phys. D: Appl. Phys.* **40** 960
[41] Chen P, Wu R X, Xu J, Jiang A M and Ji X Y 2007 *J. Phys.: Condens. Matter* **19** 106205
[42] Chen S W, Du J J, Liu S Y, Lin Z F and Chui S T 2008 *Opt. Lett.* **33** 2476

[43] Chen S W, Du J J, Liu S Y, Lin Z F and Chui S T 2008 *Phys. Rev. A* **78** 043803
[44] Liu S Y, Du J J, Lin Z F, Wu R X and Chui S T 2008 *Phys. Rev. B* **78** 155101
[45] van de Hulst H C 1957 *Light Scattering by Small Particles* (New York: John Wiley & Sons)
[46] Ruan Z and Fan S 2010 *Phys. Rev. Lett.* **105** 013901
[47] Ruan Z and Fan S 2011 *Appl. Phys. Lett.* **98** 043101
[48] Du J J, Lin Z F, Chui S T, Lu W L, Li H, Wu A M, Sheng Z, Zi J, Wang X, Zou S C and Gan F W 2011 *Phys. Rev. Lett.* **106** 203903
[49] Eggimann W H 1960 *IEEE Trans. Microwave Theory Techol.* **8** 440
[50] Ho K M, Chan C T and Soukoulis C M 1990 *Phys. Rev. Lett.* **65** 3152
[51] Chan C T, Yu Q L and Ho K M 1995 *Phys. Rev. B* **51** 16635
[52] Moroz A 2002 *Phys. Rev. B* **66** 115109
[53] Lin Z F and Chui S T 2004 *Phys. Rev. E* **69** 056614
[54] Liu S Y and Lin Z F 2006 *Phys. Rev. E* **73** 066609
[55] Liu S Y and Lin Z F 2006 *Eur. Phys. J. B* **53** 301
[56] Li L M and Zhang Z Q 1998 *Phys. Rev. B* **58** 9587
[57] Leung K M and Qiu Y 1993 *Phys. Rev. B* **48** 7767
[58] Quinten M, Leitner A, Krenn J R and Aussenegg F R 1998 *Opt. Lett.* **23** 1331
[59] Liu S Y, Chen W K, Du J J, Lin Z F, Chui S T and Chan C T 2008 *Phys. Rev. Lett.* **101** 157407
[60] Lin Z F and Chui S T 2007 *Opt. Lett.* **32** 2288
[61] Jin J F, Liu S Y, Lin Z F and Chui S T 2009 *Phys. Rev. B* **80** 115101
[62] Verslegers L, Yu Z F, Ruan Z C, Catrysse P B and Fan S H 2012 *Phys. Rev. Lett.* **108** 083902
[63] Tribelsky M and Lukyanchuk B 2006 *Phys. Rev. Lett.* **97** 263902
[64] Liu Z, Lin Z F and Chui S T 2004 *Phys. Rev. E* **69** 016619
[65] The lattice sum $S(n)$ here differs from that in the conventional MST (see, e.g., [66]) by a factor $e^{in\phi_k}$, so that the structure factor $A(n)$ becomes real symmetric.
[66] Chui S T and Lin Z F 2008 *Phys. Rev. E* **78** 065601
[67] Fukui T, Hatsugai Y and Suzuki H 2005 *J. Phys. Soc. Jpn.* **74** 1674
[68] Hatsugai Y, Fukui T and Suzuki H 2006 *Physica E* **34** 336
[69] Rikken G L J A and van Tiggelen B A 1996 *Nature* **381** 54
[70] Haldane F D M and Raghu S 2008 *Phys. Rev. Lett.* **100** 013904
[71] Wang Z, Chong Y D, Joannopoulos J D and Soljacic M 2008 *Phys. Rev. Lett.* **100** 013905
[72] Wang Z, Chong Y D, Joannopoulos J D and Soljačić M 2009 *Nature* **461** 772
[73] Ao X Y, Lin Z F and Chan C T 2009 *Phys. Rev. B* **80** 033105
[74] Poo Y, Wu R X, Lin Z F, Yang Y and Chan C T 2011 *Phys. Rev. Lett.* **106** 093903
[75] Chui S T and Lin Z F 2007 *J. Phys.: Condens. Matter* **19** 406233
[76] Chui S T and Lin Z F 2010 *J. Phys.: Condens. Matter* **22** 182201
[77] Liu S Y, Lu W L, Lin Z F and Chui S T 2010 *Appl. Phys. Lett.* **97** 201113
[78] Liu S Y, Lu W L, Lin Z F and Chui S T 2011 *Phys. Rev. B* **84** 045425
[79] Shen J, Liu S Y, Zhang H W, Chui S T, Lin Z F, Fan X, Kou X M, Lu Q and Xiao J Q 2012 *Plasmonics* **7** 287
[80] Poo Y, Wu R X, Liu S Y, Lin Z F and Chui S T 2012 *Appl. Phys. Lett.* **101** 081912
[81] Fu J X, Liu R J and Li Z Y 2010 *EPL* **89** 64003
[82] Fu J X, Liu R J and Li Z Y 2010 *Appl. Phys. Lett.* **97** 041112
[83] Lian J, Fu J X, Gan L and Li Z Y 2012 *Phys. Rev. B* **85** 125108
[84] Wolf S A, Awschalom D D, Buhrman R A, Daughton J M, von Molnar S, Roukes M L, Chtchelkanova A Y and Treger D M 2001 *Science* **294** 1488
[85] Zutic I, Fabian J and Das Sarma S 2004 *Rev. Mod. Phys.* **76** 323
[86] Jedema F J, Filip A T and van Wees B J 2001 *Nature* **410** 345
[87] Jedema F J, Heersche H B, Filip A T, Baselmans J J A and van Wees B J 2002 *Nature* **416** 713
[88] Kimura T, Hamrle J, Otani Y, Tsukagoshi K and Aoyagi Y 2004 *Appl. Phys. Lett.* **85** 3501
[89] Ji Y, Hoffmann A, Pearson J E and Bader S D 2006 *Appl. Phys. Lett.* **88** 052509
[90] Zou H, Chui S T, Wang X J and Ji Y 2011 *Phys. Rev. B* **83** 094402
[91] Kane C L and Mele E J 2005 *Phys. Rev. Lett.* **95** 226801
[92] Kajiwara Y, Harii K, Takahashi S, Ohe J, Uchida K, Mizuguchi M, Umezawa H, Kawai H, Ando K, Takanashi K, Maekawa S and Saitoh E 2010 *Nature* **464** 262
[93] Liu T and Vignale G 2011 *Phys. Rev. Lett.* **106** 247203
[94] Fan X and Xiao J Q 2014 unpublished
[95] Walker M B 1971 *Phys. Rev. B* **3** 30
[96] Silsbee R H, Janossy A and Monod P 1979 *Phys. Rev. B* **19** 4382
[97] Chui S T and Lin Z F 2008 *Phys. Rev. B* **77** 094432
[98] Chen Y P, Fan X, Chui S T and Xiao J Q unpublished
[99] Allen L, Padgett M J and Babiker M 1999 *Prog. Opt.* **39** 291
[100] Soskin M S and Vasnetsov M V 2001 *Prog. Opt.* **42** 219
[101] Yao A M and Padgett M J 2011 *Adv. Opt. Photon* **3** 161
[102] Dholakia K and Cizmar T 2011 *Nat. Photonics* **5** 335
[103] MacDonald M P, Paterson L, Volke-Sepulveda K, Arlt J, Sibbett W and Dholakia K 2002 *Science* **296** 1101
[104] Padgett M and Bowman R 2011 *Nat. Photonics* **5** 343
[105] Paterson L, MacDonald M P, Arlt J, Sibbett W, Bryant P E and Dholakia K 2001 *Science* **292** 912
[106] Barreiro J T, Wei T C and Kwiat P G 2008 *Nat. Phys.* **4** 282
[107] Nagali E, Sansoni L, Sciarrino F, De Martini F, Marrucci L, Piccirillo B, Karimi E and Santamato E 2009 *Nat. Photonics* **3** 720
[108] Molina-Terriza G, Torres J P and Torner L 2007 *Nat. Phys.* **3** 305
[109] Leach J, Jack B, Romero J, Jha A K, Yao A M, Franke-Arnold S, Ireland D G, Boyd R W, Barnett S M and Padgett M J 2010 *Science* **329** 662
[110] Bernet S, Jesacher A, Furhapter S, Maurer C and Ritsch-Marte M 2006 *Opt. Express* **14** 3792
[111] Elias N M 2008 *Astron. Astrophys.* **492** 883
[112] Ng J, Lin Z F and Chan C T 2010 *Phys. Rev. Lett.* **104** 103601
[113] Wang J, Yang J Y, Fazal I M, Ahmed N, Yan Y, Huang H, Ren Y X, Yue Y, Dolinar S, Tur M and Willner A E 2012 *Nat. Photonics* **6** 488
[114] Gibson G, Courtial J, Padgett M J, Vasnetsov M, Pasko V, Barnett S M and Franke-Arnold S 2004 *Opt. Express* **12** 5448
[115] Chui S T and Lin Z F 2014 *Opt. Lett.* **39** 5732
[116] See, e.g., Harada Y and Asakura T 1996 *Opt. Commun.* **124** 529
[117] See, for example, Albaladejo A, Marques M I, Laroche M and Saenz J J 2009 *Phys. Rev. Lett.* **102** 113602
[118] See, for example, Jackson J D 1999 *Classical Electrodynamics* (3rd edn.) (New York: John Wiley) p. 308